THE EFFECTS OF TURBULENCE STRUCTURES ON THE AIR-SIDE PERFORMANCE OF COMPACT TUBE-FIN HEAT EXCHANGERS

By

Colin Bidden Allison

A Thesis submitted in fulfilment of the requirements for the
Degree of Doctor of Philosophy

SCHOOL OF MECHANICAL ENGINEERING

UNIVERSITY OF ADELAIDE

June 2006

© Colin Bidden Allison

Chapter 4

Numerical Simulation Methodology

4.1   Introduction

Numerical simulation of tube-fin heat exchanger performance is quite prevalent in the literature, and excellent agreement with experimental data has been achieved. There is some diversity in the treatment of heat exchanger modelling however, with respect to the type of model selected and stipulation of the boundary conditions. For example the question of flow character occurring within the model is debatable. Many argue that the flow should be considered laminar due to the small length scales occurring between fins. Conversely it has also been shown that flow unsteadiness occurs at low Reynolds numbers due to the surface roughness, louvres and other effects. Hence turbulent models are preferred. The k-ε turbulence models appear to be the most widely used, although more recently the LES turbulence model has shown to provide excellent results as well as coherent visual comparisons. The commercial code FLUENT[69] has been used to perform the various CFD simulations presented here, and the pre-processing tool GAMBIT[75] was used to create the geometry as well as generate the mesh. A detailed description of the Numerical technique used in the current study follows. For convenience, the numerical parameters, modelling options and boundary conditions have been summarised and a table providing quick reference of this information can be found in Appendix III.

4.2   Turbulence Models

4.2.1   RANS Type Turbulence Models

The Reynolds averaged Navier Stokes(RANS) equations are described below in Cartesian tensor form as the instantaneous continuity equation

$$\frac{\partial p}{\partial t} + \frac{\partial}{\partial x_i}\left(\rho u_i\right) = 0 \tag{1.1}$$

and the ensemble-averaged momentum equation

$$\frac{\partial}{\partial t}\left(\rho u_i\right) + \frac{\partial}{\partial x_j}\left(\rho u_i u_j\right) = \frac{\partial p}{\partial x_i} + \frac{\partial}{\partial x_j}\left[\mu\left(\frac{\partial u_i}{\partial x_j} + \frac{\partial u_j}{\partial x_i} - \frac{2}{3}\delta_{ij}\frac{\partial u_l}{\partial x_l}\right)\right] + \frac{\partial}{\partial x_j}\left(-\rho\overline{u_i'u_j'}\right) \tag{1.2}$$

The term $-\rho\overline{u^i u^j}$ represents the Reynolds stresses which need to be modelled in order to close Equation(1.2). The Boussinesq hypothesis is commonly used to relate the Reynolds stresses to the mean velocity gradients as:

$$-\rho\overline{u^i u^j} = \mu_t\left(\frac{\partial u_i}{\partial x_j} + \frac{\partial u_j}{\partial x_i}\right) - \frac{2}{3}\left(\rho k + \mu_t\frac{\partial u_i}{\partial x_i}\right) \tag{1.3}$$

The Boussinesq hypothesis is used in several types of turbulence model including the range of k-ε turbulence models. The realizable k-ε turbulence model has been adopted for the simulations performed throughout this body of work. The reason behind this choice and a description of the model is provided later. For transient simulations the LES turbulence model has been adopted.

4.2.1.1   Realizeable k-ε Turbulence Model

The term realizable means the model satisfies certain mathematical constraints on the Reynolds stresses, consistent with the physics of turbulent flows[69]. It is likely to provide superior performance for flows involving separation and recirculation. Of all the k-ε model versions, it has shown the best performance for several validations of separated flows and flows with complex secondary flow features.

The modelled transport equations for k and ε are:

$$\frac{\partial}{\partial t}\left(\rho k\right) + \frac{\partial}{\partial x_i}\left(\rho k u_j\right) = \frac{\partial}{\partial x_i}\left[\left(\mu + \frac{\mu_t}{\sigma_k}\right)\frac{\partial k}{\partial x_j}\right] + G_k + G_b - \rho\varepsilon - Y_M + S_k \tag{1.4}$$

and

$$\frac{\partial}{\partial t}(\rho\varepsilon) + \frac{\partial}{\partial x_j}(\rho\varepsilon u_j) = \frac{\partial}{\partial x_j}\left[\left(\mu + \frac{\mu_t}{\sigma_\varepsilon}\right)\frac{\partial\varepsilon}{\partial x_j}\right] + \rho C_1 S\varepsilon - \rho C_2 \frac{\varepsilon^2}{k + \sqrt{\nu\varepsilon}} + C_{1\varepsilon}\frac{\varepsilon}{k} - C_{3\varepsilon}G_b + S_\varepsilon$$

(1.5)

where,

$$C_1 = \max\left[0.43, \frac{\eta}{\eta + 5}\right], \qquad \eta = S\frac{k}{\varepsilon}$$

The eddy viscosity is computed from

$$\mu_t = \rho C_\mu \frac{k^2}{\varepsilon}$$

(1.6)

The term C_μ is no longer constant, as it is in the other k-ε models, but is computed from

$$C_\mu = \frac{1}{A_0 + A_s \frac{kU^*}{\varepsilon}}$$

(1.7)

where,

$$U^* \equiv \sqrt{S_{ij}S_{ij} + \widetilde{\Omega}_{ij}\widetilde{\Omega}_{ij}}$$

(1.8)

and,

$$\widetilde{\Omega}_{ij} = \Omega_{ij} - 2\varepsilon_{ijk}\omega_k$$

$$\Omega_{ij} = \overline{\Omega}_{ij} - \varepsilon_{ijk}\omega_k$$

where, $\overline{\Omega}_{ij}$ is the mean rate-of-rotation tensor viewed in a rotating reference frame with the angular velocity ω_k. The model constants A_0 and A_s are given by

$$A_0 = 4.04, \text{ and } A_s = \sqrt{6}\cos\phi$$

where,

$$\phi = \frac{1}{3}\cos^{-1}\left(\sqrt{6}W\right), \qquad W = \frac{S_{ij}S_{jk}S_{ki}}{S}, \qquad \widetilde{S} = \sqrt{S_{ij}S_{ij}}, \qquad S_{ij} = \frac{1}{2}\left(\frac{\partial u_j}{\partial x_i} + \frac{\partial u_i}{\partial x_j}\right)$$

The model constants C_2, σ_k, and σ_ε have been established to ensure that the model performs well for certain canonical flows. The model constants are

$$C_{1\varepsilon} = 1.44\,, \qquad C_2 = 1.9\,, \qquad \rho_k = 1.0\,, \qquad \rho_\varepsilon = 1.2$$

4.2.1.2   LES turbulence models

Large Eddy Simulation is a combination of Direct Numerical Simulation (DNS) and RANS type models. Large eddies are resolved directly in LES, while small eddies are modelled. Most of the momentum, mass, energy, and other scalers are transported by large eddies. Large eddies are more problem dependent. They are dictated by the geometries and boundary conditions of the flow involved. Small eddies are less dependent on the geometry, tend to be more isotropic, and are consequently more universal. Solving only for the large eddies and modelling the smaller scales results in mesh resolution requirements that are much less restrictive than with DNS. Typically, mesh sizes can be at least one order of magnitude smaller than with DNS. Furthermore since the time step size is determined by the eddy-turnover time, this requirement is much less restrictive than with DNS. In practical terms, however, extremely fine meshes are still required. LES modelling is currently still expensive in terms of computing requirements.

The governing equations employed for LES are obtained by filtering the time-dependent Navier-Stokes equations. The filtering process effectively filters out the eddies, whose scales are smaller than the filter width or grid spacing used in the computations.

In order to obtain a stable solution for transient modelling the time step size required must be below the following limit:

$$\delta t \leq \frac{1}{\left|\delta x / u\right| + \left|\delta y / v\right|} \tag{1.9}$$

This condition is referred to as the Courant-Friedrichs-Lewy (CFL) condition[69]. Hence the time step size can be calculated from the CFL number:

$$CFL = \left(\frac{\Delta t . u_{max}}{\Delta x} \right) \qquad (1.10)$$

By enabling the **Data Sampling for Time Statistics** option FLUENT will gather data for time statistics while performing a large eddy simulation. The mean and the root-mean-square (RMS) values are then viewed.

4.3   Modelling Heat Transfer

The form of the energy equation that applies is:

$$\frac{\partial}{\partial t}(\rho E) + \frac{\partial}{\partial x_i}(u_i(\rho E + p)) = \frac{\partial}{\partial x_i}\left(k_{eff} \frac{\partial T}{\partial x_i} \right) \qquad (1.11)^1$$

Where k_{eff} is the effective conductivity $(k+k_{t,})$ where k_t is the turbulent thermal conductivity, defined according to the turbulence model being used.

E is the total Energy defined by

$$E = h - \frac{p}{\rho} + \frac{\upsilon^2}{2} \qquad (1.12)$$

For the solid regions such as struts or fins the following energy transport equation is used:

$$\frac{\partial}{\partial t}(\rho c_p T) = \frac{\partial}{\partial x_i}\left(k_s \frac{\partial T}{\partial x_i} \right) \qquad (1.13)$$

The heat transfer through the inlet and outlet surfaces was computed by integrating the cell values across the surface using the following expression:

$$Q = \int H \rho \vec{\upsilon}.d\vec{A} \qquad (1.14)$$

where H is the total enthalpy.

---

[1] Note that buoyancy and radiation effects have been neglected.

4.4   CFD modelling procedure

In addition to modelling the various coil prototypes, the two commercial louvre fin surfaces were also modelled. Since experimentally measured performance results have been obtained for these coils, the simulation validation can be extended to include these results. One option was to model the fins as flat plates and then introduce a surface roughness factor to account for the presence of the louvres. However this approach did not yield an acceptable comparison with experimental values, particularly with respect to the pressure drop. Therefore in order to ensure sufficient detail was included in the modelling, the louvres were accurately depicted in the fin surface geometry as shown in Figure 4.4.1 which shows the extent of the model computational domain.
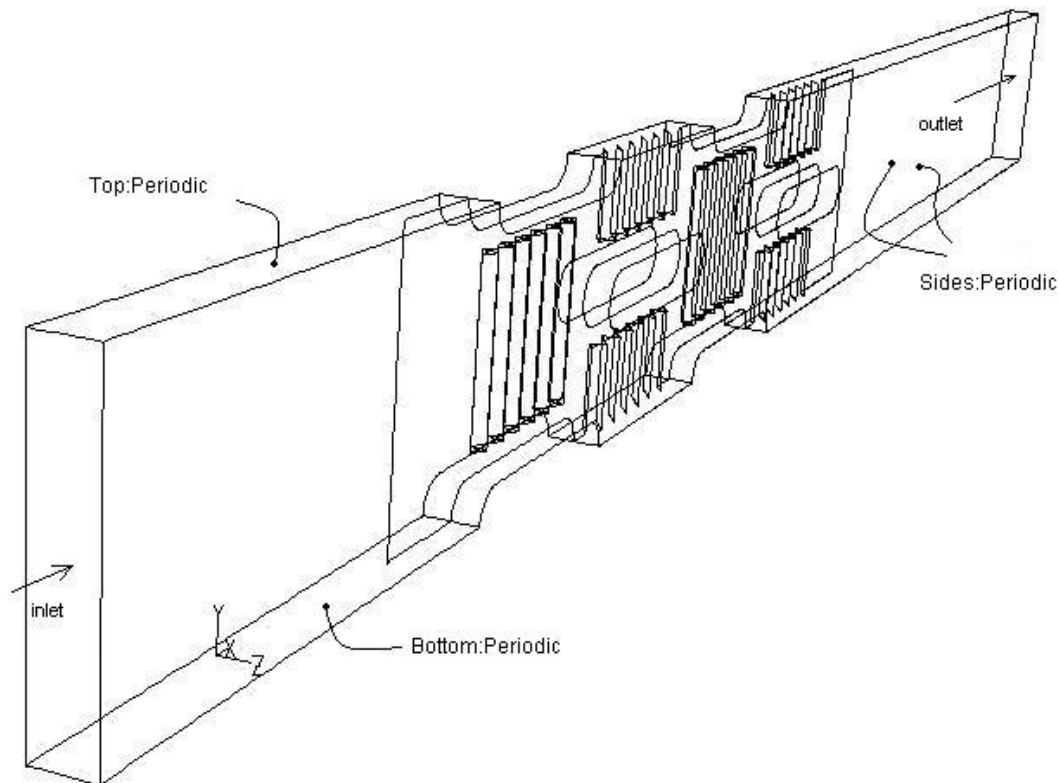
Figure 4.4.1 Sketch of the louvre fin computational domain and boundary conditions

4.4.1   Computational Domain

The width of the domain for each of the two louvre fin coils was kept synonymous to their fin pitch, 2.31mm for the 11fpi coil and 2.82mm for the 9fpi coil. The length

dimensions were kept in proportion to the transverse tube pitch P_t=12mm. The inlet length of the domain was equal to $3P_t$ and the draught length was $4.5P_t$. The fin and tube section was equal to $5P_t$. The fin was modelled as a thin surface. The louvre surfaces, as well as the louvre landing surface were "cut or split" from the fin surface and then rotated through the required louvre angle Θ. The corresponding volumes so formed were used to split the domain so that the louvre surfaces could be defined. This also created the louvre sides, or the twist in the surface which provides the transition from fin to louvre. In the actual coils, the louvre sides are created through elastic deformation of the fin surface during the louvre rolling process. As a result the louvre sides would be expected to be thinner than the corresponding fin material, and this was accounted for in the model.

4.4.2   Mesh Structure

For these series of models the domain was meshed with a hybrid mesh consisting of both a structured and tetrahedral mesh. Before each domain was meshed, a boundary layer was applied to the tube surfaces. The boundary layer mesh consisted of 6 layers of a 0.1mm thick cell. Figure 4.4.2 shows a detail of the Boundary Layer mesh existing around each tube face.
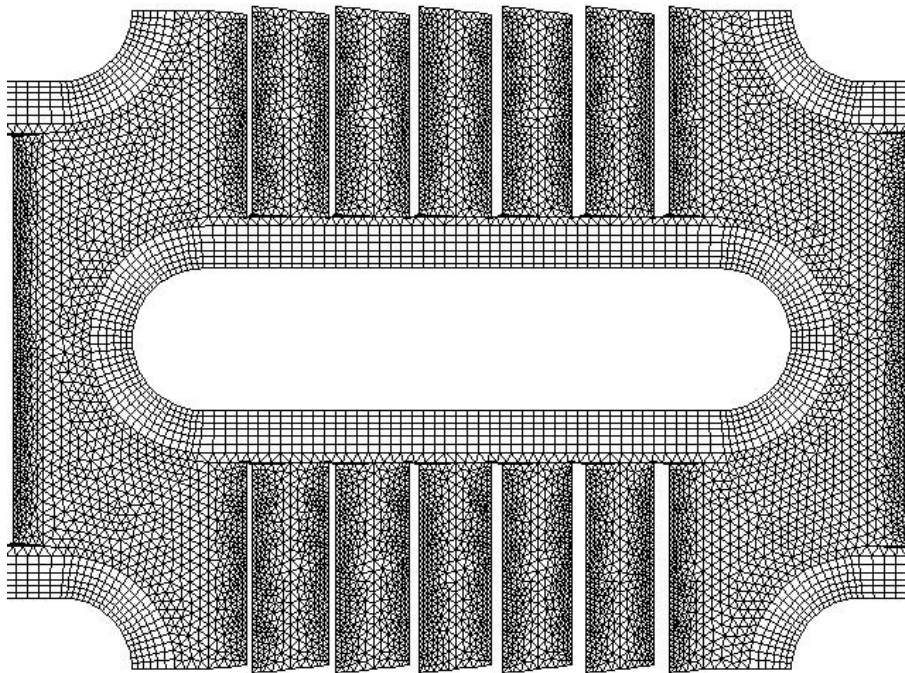

Figure 4.4.2 Close up view of the mesh around the tubes, showing the extent of Boundary Layer mesh

The inlet and draught sections were meshed with a sub-mappable hex mesh, consisting of cell size measuring 0.2mm by 0.4mm. The fin, louvre and tube section was meshed with a tetrahedral mesh varying in cell size. The louvre edges were pre-meshed with a 0.1mm edge mesh. Size functions were implemented to control the growth of cells from the louvre edges having 0.1mm cells to the outer regions where the cell size was 0.2mm. It was necessary to refine the mesh in the vicinity of the louvres since additional turbulence, and flow separation would be expected to occur as a result of their presence. Figure 4.4.3 shows a detail of the louvre array indicating the refinement of the tetrahedral mesh used to wrap the fin surface.
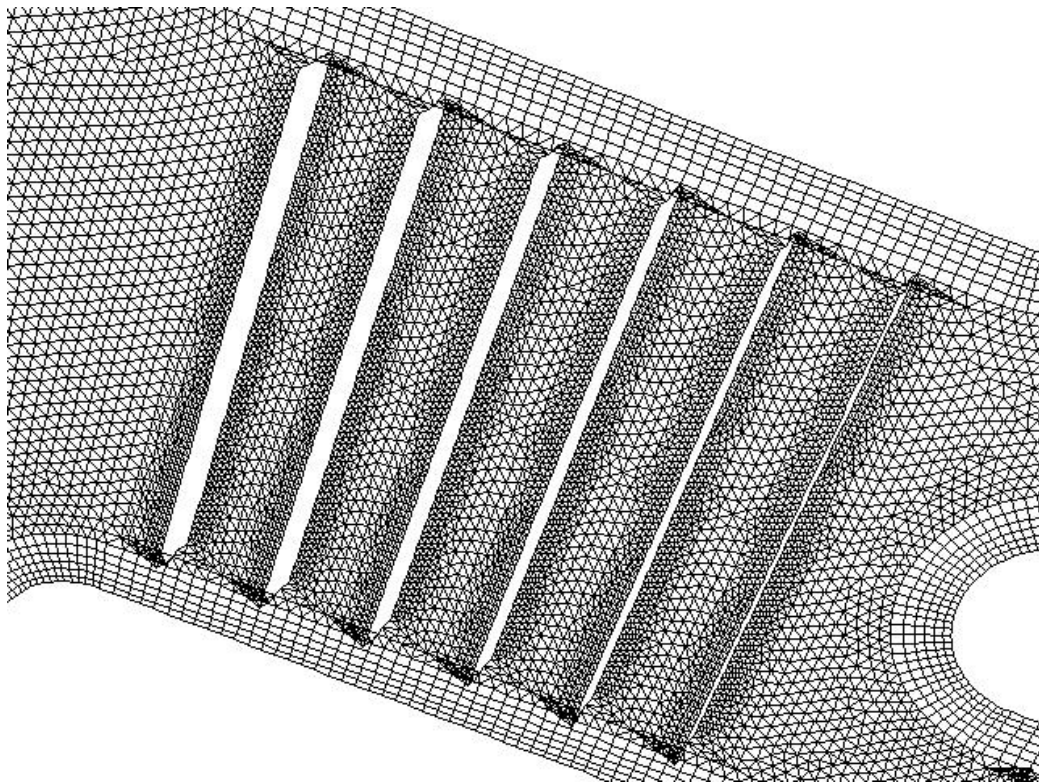
Figure 4.4.3 Close up view showing the tetrahedral mesh spread over the louvres and louvre sides.

4.4.3 Boundary Conditions

Boundary conditions were selected to be synonymous with the actual flow conditions used for testing the experimental coil prototypes so that the Reynolds numbers and *LMTD*'s were similar. The boundary condition values such as velocity and temperature settings were kept identical for each simulation, so that direct

comparisons could be made. The only exception with respect to the selection of a type of boundary condition occurs for the conditions at the model boundaries, being either symmetrical or periodic, and this is discussed in Section 4.4.5. The typical boundary conditions are pictorially represented in Figure 4.4.1.

4.4.3.1 Inlet boundary conditions

At the upstream inlet surface, the dry air entering the computational domain is specified to have uniform velocity u_{in} with values of 6.3, 4.8 or 2.9m/s. The air is assumed to be an incompressible ideal gas and the thermo physical properties, density, viscosity, thermal conductivity and specific heat are selected from the FLUENT default values. The inlet temperature T_{in} was specified to be the same as the actual experimental conditions of 40 degrees Celsius (313 K). The turbulent intensity I was specified as 5%. The velocity components in the y and z directions are considered to be zero. The hydraulic diameter necessary in order to set the appropriate turbulence scale was specified as equal to the model width in each case.

4.4.3.2 Outlet Boundary Conditions

This surface was designated as a pressure outlet, with the default pressure level set at ambient conditions, or 0 Pa. Thus by computing the pressure at the inlet surface, the pressure drop across the coil is obtained. The backflow turbulent intensity was specified as 15%. Similarly the backflow hydraulic diameter was specified as equal to the model width in each case.

4.4.3.3 Wall Boundary Conditions

At the solid surfaces, the fins, struts and tubes, the no-slip boundary condition has been enforced. For the models containing struts with a finite thickness containing volumes, these were specified as solid continuum types. A solid region contains cells for which only a heat conduction problem is solved; no flow equations are solved. The material for the solid region was specified as brass, or copper as required. For the case of thin surfaces such as standard copper fins, these have been modelled using the shell conduction option. Modelling the struts as a thin surface with zero finite thickness is a

convenient feature accessible in the FLUENT software. By selecting the shell conduction option, conjugate heat transfer can be accommodated. Although the surface thickness is not physically modelled, its thickness must be specified to calculate the one-dimensional heat conduction. This saves computational expense, where the thickness of the sheets is not expected to significantly alter the fluid flow characteristics, but conduction through the shell is required. This was considered a valid assumption considering that the modelled fin thickness was 0.076mm thick.

The tube faces were specified as a fixed temperature surface, equal to the experimental chilled water value of 284.5 K (11.5 degrees Celsius). This modelled boundary condition would apply uniformly over the entire tube surface, unlike the actual boundary condition on the tube surface which is not constant during the experiment. This introduces an error into the modelling procedure, which would cause a departure from the physically real conditions. Therefore comparison with experimental conditions in this case is not applicable. However since the width of the model is small the error in assuming a constant surface temperature is minimal. Furthermore, since the same error is applied to all simulations, one can still expect excellent comparisons between the various models. By normalising the results of both Numerical and experimental results, an excellent and valuable comparison can be made. Indeed, in this way the experimental values can be used to validate the integrity of the Numerical simulations.

4.4.4 Near Wall Treatment

The k-ε turbulence models and the LES model in FLUENT are primarily valid for turbulent core flows, occurring somewhat far from any walls. A modelling approach is therefore required to make these models suitable for wall-bounded flows. The flow adjacent to a wall, the near wall region can be subdivided into three regions. Nearest to the wall the flow is almost laminar and forms the "viscous sublayer". In this region viscosity plays a dominant role in momentum and heat transfer. Furthest from the wall is the outer layer or fully-turbulent layer where turbulence plays a major role. Between these two regions is an interim region or buffer layer where the effects of viscosity and turbulence are equally important. These subdivisions are sketched in Figure 4.4.4 which shows the structure of the typical turbulent velocity profile in a non dimensional form plotted as a function of the non dimensional distance from the

wall y^+. In the viscous sublayer the velocity profile can be written in dimensionless form as

$$\frac{\overline{u}}{u^*} = \frac{yu^*}{\nu} = y^+ \qquad\qquad (1.15)$$

Where $y=R\text{-}r$ is the distance measured from the wall, $\overline{u}$ is the time-averaged $x-component$ of velocity, and u^* is termed the friction velocity. Equation (1.15) is commonly called the law of the wall and is valid very near the smooth wall for $0 \le y^+ \le 5$ [76].

NOTE:
This figure is included on page 96
of the print copy of the thesis held in
the University of Adelaide Library.

Figure 4.4.4 Sketch showing the subdivisions of the Near-Wall Region[69]

Traditionally there are two approaches to modelling the near wall region. In one approach the inner and buffer layers are not resolved numerically. Instead, semi-emperical formulas called "wall functions" are used to bridge the viscosity-affected region between the wall and the fully-turbulent region. In the other approach the turbulence models are modified to enable the viscosity-affected region to be modelled all the way to the wall including the viscous sublayer. The wall function approach is inadequate in situations where the low-Reynolds number effects are pervasive in the flow domain in question, and the hypotheses underlying the wall functions cease to be valid. For these cases near wall models are required to be integrable all the way to the

wall, and the mesh has to be fine enough to resolve the laminar sublayer (typically $y^+ \approx 1$). Fluent offers several options with respect to treating the near wall regions including an enhanced wall treatment. This combines a two-layer approach with enhanced wall functions. It is designed to accommodate meshes that vary in size and which may not be fine enough close to the wall. Since the majority of the computational domains modelled in this study have been meshed with a tetrahedral mesh which varies in size, the enhanced wall treatment has been used throughout. However, as previously mentioned, a requirement of this approach is that the mesh at least be fine enough so, that $y^+ \leq 5$. For each case, the y^+ values were verified by plotting these after simulation convergence, such as the example shown in Figure 4.4.5.
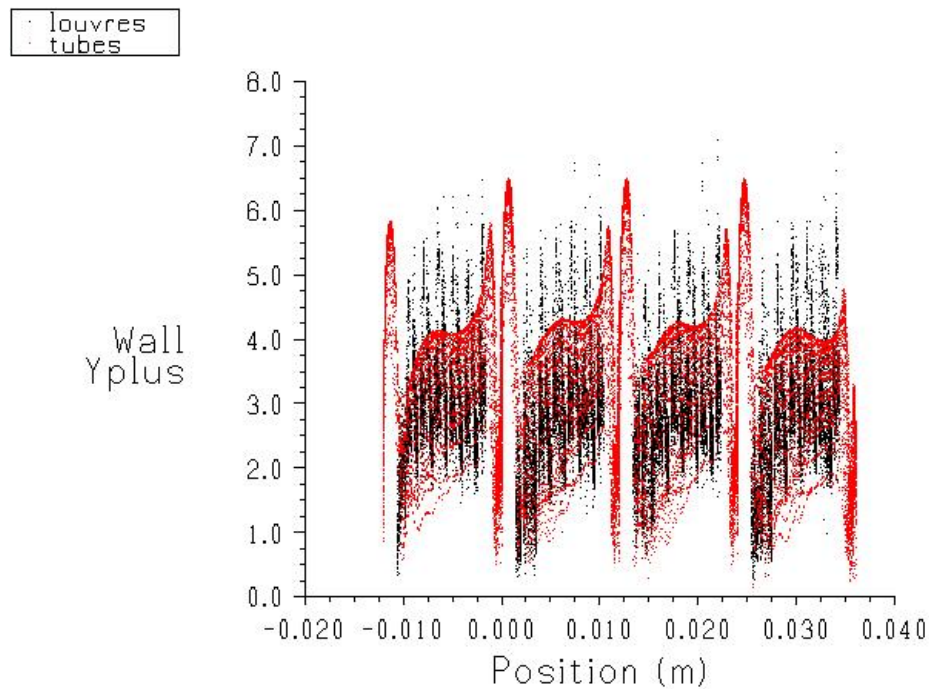
Figure 4.4.5 Plot of the y^+ values occurring on the tube and louvre surfaces for the computational domain of the louvre fin surface with an inlet velocity of 6.3m/s. The black zones correspond to the louvre surfaces, and the red zones cover the tube surfaces

It is evident in this figure that the majority of the y^+ values are less than 5. The 8 red peaks correspond to the tube stagnation points and wake zones, and the six black

peaks correspond to the 5 louvre leading edges and the landing leading edge. Since all the values are less than 7, the refinement of the mesh on the louvre edges appears to be sufficient, even at the maximum velocity of 6.3*m/s*.

4.4.5   Periodic versus Symmetry Boundary Conditions

The choice of fluid boundary conditions for geometrically similar computational domains requires careful consideration. A reasonable knowledge of the flow distribution is required *a priori* since a symmetrical domain does not necessarily mean a symmetrical flow. Figure 4.4.6 is a simple sketch which explains the difference between periodic and symmetry boundary conditions.
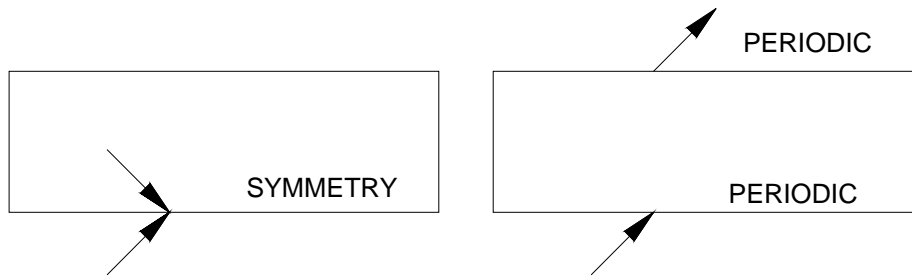
Figure 4.4.6 Sketch explaining the difference between periodic and symmetry boundary conditions

Periodic boundary conditions are used when the physical geometry of interest and the expected pattern of flow/thermal solution have a periodically repeating nature. At a periodic boundary the transport variables are allowed to cross the boundary in a repeating fashion. At a symmetry boundary on the other hand there is no convective flux across the boundary, and the velocity gradients normal to the boundary are zero.

With respect to the range of models having louvred fins which are simulated in this project, the choice of boundary conditions for the sides of the model (refer to Figure 4.4.1) depends on the geometry where louvres are modelled. If the louvre direction of adjacent fins is mirrored, then symmetry conditions are required. If the louvre direction is repeated between successive fins, then a periodic boundary condition would

be the appropriate selection. In most cases periodic conditions have been used for the side boundaries.

4.4.6 Numerical Schemes

The equations presented in Sections 4.2 and 4.3 have been discretised using the Finite Volume Technique. Since the field variables are stored at the cell centres, their values must be interpolated to the cell faces. For the convection terms the Second-Order Upwind Scheme has been used to interpolate the field variables.
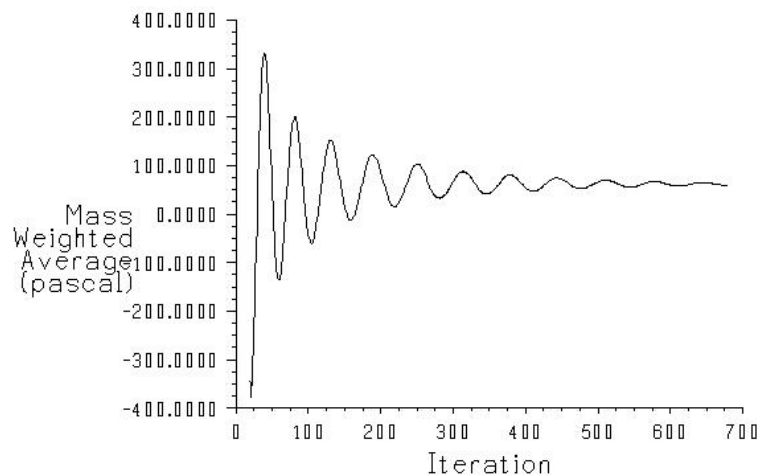
The Segregated (implicit) solver which has been used to solve the equations, has additional interpolation options, such as face pressure, for which the Standard scheme has been used. In addition, the segregated solver includes a numerical algorithm or Pressure-Velocity coupling which uses a combination of continuity and momentum equations to derive an equation for pressure correction. The default scheme SIMPLE has been used for the pressure-velocity coupling. For the unsteady simulations the Pressure-Implicit with Splitting of Operators or PISO scheme was adopted. The PISO scheme is based on the SIMPLE scheme but is based on the higher degree of the approximate relation between the corrections for velocity and pressure. The PISO algorithm performs two additional corrections: neighbour correction and skewness correction. It improves the efficiency of calculations, and is particularly suited to unsteady flow problems or meshes containing a higher than average skew[69].

4.4.7 Solution Accuracy

Clearly the fidelity of the numerical solution depends on the quantity of cells or the minimum cell size used throughout the computational domain. Computational time and memory limitations restrict the degree of cell refinement to practical levels. However the mesh density was refined in areas where it was needed to resolve salient flow features such as in tube wakes or louvre edges and the like. In addition Grid Independence studies were conducted in order to determine the adequate mesh size, and this is described in Chapter 6. Caution had to be exercised to minimise extreme variations in cell size in non-uniform meshes. This is necessary in order to minimise truncation error. Furthermore the mesh quality was inspected in each case to minimise cell skewness and aspect ratio. In the case of a structured mesh, the grid was aligned with the flow direction in order to minimise "false diffusion". In the case of tetrahedral

cells the skewness was limited to a ratio of 0.85, while for structured meshes this restriction could be relaxed to a ratio of 0.9. Numerical errors are associated with calculation of cell gradients and cell face interpolations. In order to contain numerical errors a higher order discretization scheme, the second-order upwind scheme, was used for all cases.

In order to monitor convergence, residual plots based on the FLUENT default tolerance for the residual values have been used. This criterion requires that the scaled residuals decrease to 10^{-3} for all equations except the energy equation for which the criterion is 10^{-6}. Residual definitions that are useful for one class of problem are sometimes misleading for other classes of problems. Therefore it was considered prudent to judge convergence by monitoring relevant integrated quantities such as pressure or temperature. Hence in each case the mass weighted surface integral of static pressure at the inlet boundary was plotted. In some instances, although the default convergence criterion was achieved, the inlet surface pressure integral showed oscillating values which decay but do not level out as shown in Figure 4.4.7. This indicates that convergence has not been achieved. Hence the convergence criterion was reduced to 10^{-4} and additional iterations performed in order to achieve convergence. This was realised when the oscillating mass weighted surface integral of inlet pressure had stabilised to reflect a constant value.

Figure 4.4.7 Plot of pressure oscillations at inlet boundary

Another check for solution accuracy was the overall heat and mass balance between inlet and outlet flow surfaces. Overall heat and mass balances were monitored to ensure that a net imbalance of less than 1% of the smallest flux through the domain boundary was achieved in all cases. Typically the mass imbalance between inlet and outlet boundaries was in the order of 10^{-8}.

In some cases where convergence was sluggish the under-relaxation factor for momentum, was reduced in order to hasten convergence. However this is not expected to affect solution accuracy.

A solution is said to be independent when any further reduction in cell size results in no further change in solution to within an acceptable tolerance. A grid independence study has been performed for a particular range of models, and is reported in the applicable section.

For the LES simulations, initially a steady state solution was reached. This solution was then used as a starting point for the unsteady simulations. This was done in order to minimise the time required for the flow to develop. If an appropriate time step was used then the solution would converge within 20 iterations. The simulations were run by selecting enough time steps to allow for approximately 2-3 seconds of flow time to ensure that the flow was fully developed. The flow development was monitored by observing the residual plots as well as animations set up to display transverse vorticity along a horizontal plane. At the onset of regular vortex shedding, it was clear that the flow had developed. At this point the **Data Sampling for Time Statistics** option was enabled and the simulation allowed to proceed for a reasonable time period, typically 3-4 seconds of flow time. Figure 4.4.8 is a typical plot of the residual values for an LES simulation for the case of $Sp=P_t$.
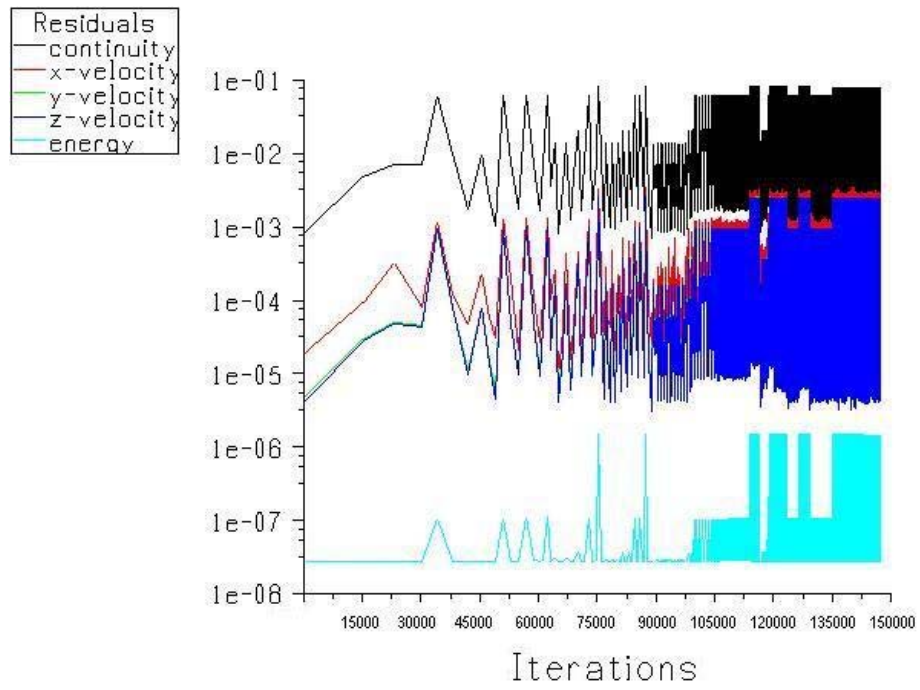
Figure 4.4.8 Plot of residual values for the LES simulation for the case of $Sp=P_t$ reaching flow development after 135000 iterations

Chapter 5

Effect of Homogeneous Turbulence on Heat Transfer and Pressure Drop

5.1   Introduction

Possibly the major disadvantage of the tube-fin heat exchanger is that the flow passages between the fins are very small. Since the fin pitch appropriately characterises the flow, the flow tends to be laminar and hence two dimensional for most air velocities, in spite of any fin surface enhancements. This limitation is particularly onerous for low Reynolds number applications. It is thought that by reconsidering the classic configuration and adopting an alternative design philosophy, these limitations might be somewhat overcome. A novel heat exchanger concept was investigated by Ko et al[59], who sough to craft a heat exchanger surface for very low Reynolds number applications. The foundation of their design was to enhance three-dimensional turbulence, and to facilitate vortex generation. The prime requisite for their design is that it has an open mesh in order to promote three dimensional turbulence. While their design was admirable, it did not distinguish between the contributions of each of the various turbulence features. This exception has motivated the current series of investigations undertaken in this work. A series of experiments have been designed to estimate the contributions of each type of turbulence mechanism. These experiments are undertaken in the context of practical heat exchanger designs. This chapter documents the experimental assessment of heat transfer potential of a heat exchanger geometry which is designed to exhibit an approximation to homogeneous turbulence. The results are compared to a standard louvre fin surface which is incorporate in an equivalent heat exchanger volume.

5.2   Prototype description

The prototype discussed in this section has been termed the Tube Mesh Heat Exchanger (TMHE). The TMHE consists entirely of flat tubing, which is arranged in alternating horizontal and vertical staggered rows, spanned between an inlet and an outlet manifold, one for each direction. Flat tubes were used since these are typically used in commercial radiator designs. Since there were several rows of horizontal and vertical tubes, the homogeneity of the flow at the flow outlet is all but guaranteed, in spite of the tubes being flat rather than round[1].
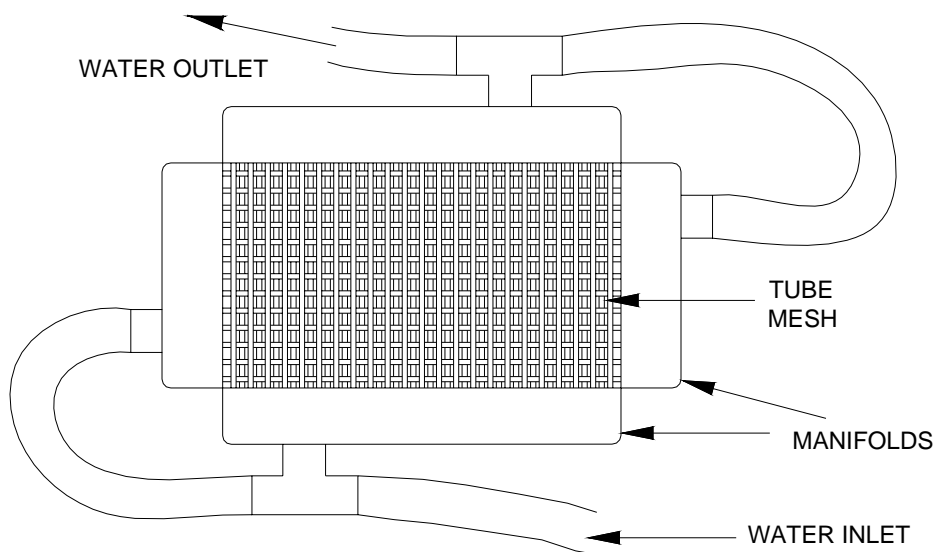
Figure 5.2.1 Sketch of the Tube Mesh Heat Exchanger

Figure 5.2.1 illustrates the arrangement schematically. There are 3 rows of horizontal tubes, 76 tubes in total[2], and there are also three rows of tubes in the vertical direction, 224 in total. Both sets of tubes are spaced at a 10mm pitch to form an open mesh. This arrangement is an insinuation of a homogeneous turbulent generating mesh similar to that described by Pope[77] and illustrated in Figure 5.2.2. Grid turbulence is an approximation to homogeneous isotropic turbulence and is the most fundamental

---

[1] A homogeneous turbulence generating grid consists typically of only one row each of horizontal and vertical circular rods (see Figure 5.2.2)
[2] Note that the standard louvre fin coils have 74 tubes, hence a slight discrepancy exists.

turbulent flow. Grid turbulence can be generated by a turbulence generating grid composed of bars at particular mesh spacing.

NOTE:
This figure is included on page 105
of the print copy of the thesis held in
the University of Adelaide Library.

Figure 5.2.2 Sketch of a homogeneous turbulence generating mesh [77]

A photograph of the face view of the coil prototype is show in Figure 5.2.3. Although the coil face area is the same as that of the standard 4 row coils, the active coil depth in this case is 73.32mm compared with 59.2mm for the standard cases. The rows of tubes running in the alternating directions have minimal contact with each other and therefore conduction between the tubes does not occur. This then forms the airside flow path. In the absence of fins, the airside convection surface area is restricted to the tube surfaces only. The chilled cooling water can then be pumped through both sets of tubes simultaneously or alternatively through either the horizontal or vertical tube bundles independently. This was facilitated by the installation of separate manifolds for each water entry and exit direction.

Figure 5.2.3 Photograph depicting the face of the Tube Mesh Heat exchanger

A close up view of the tube mesh heat exchange surface area geometry is shown in the photograph in Figure 5.2.4. Note that the tube rows are staggered in both the vertical
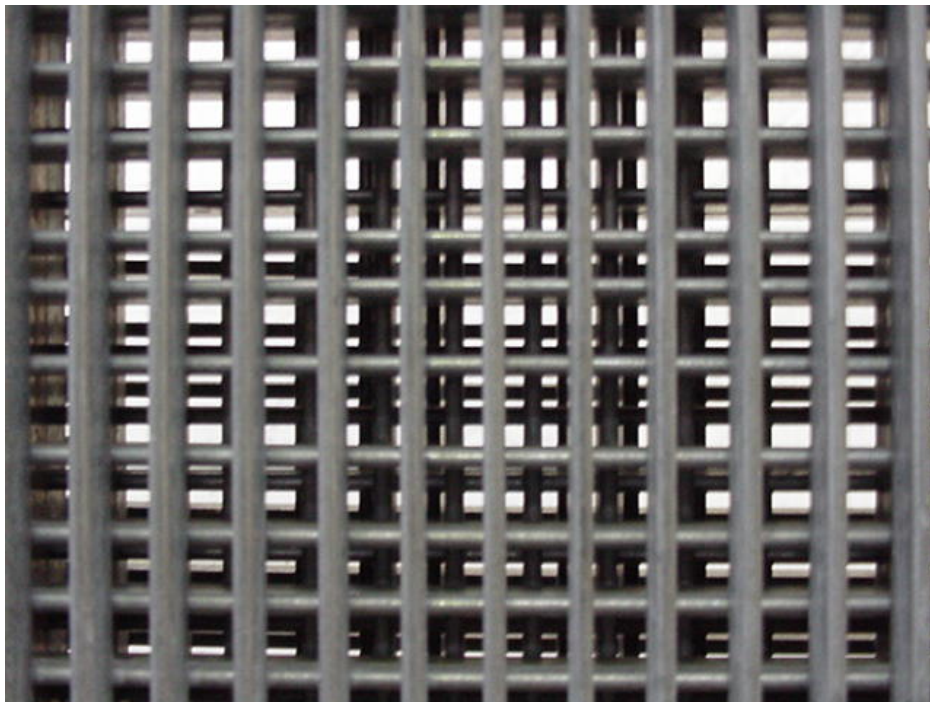
Figure 5.2.4 Close up photograph of the Tube Mesh coil

and horizontal direction to form several layers of a grid mesh.

5.3   Test Methodology

All the experimental measurements were performed using the closed circuit heat and mass flow rig located at the Thebarton Campus of the University of Adelaide. Details of the apparatus and experimental data reduction are provided in Chapter 3. Initially, it was prudent to measure the performance of louvre fin heat exchanger cores, in order to establish a performance benchmark for comparison purposes. Detailed specifications of these coils can be found in Appendix II. Essentially these coils are used for industrial radiators; they have 4 rows of compactly arranged staggered flat tubes, and have continuous copper plate fins with a louvred surface. Two standard coils were selected that were similar apart from the fin density. At 11 and 9 fins per inch, the fin densities are relatively high suggesting high performance heat exchanger coils. The measured capacity of the 11 fpi coil peaked at just over 20kW which is sufficiently large for adequate performance variation comparisons. The coils measured $760mm$ wide by $260mm$ in height providing a face area which is large in comparison to the experimental test coil sizes used by many others. This factor proportionally reduces the perimeter area serving to minimise edge losses and should improve experimental accuracy. The tubes were manifolded on either side and designed for a single circuit pure cross-flow arrangement[3]. The capacity and air pressure drop of these coils was measured over a range of air and water velocities as described below. This provided sufficient information to generate a complete performance map of each coil that covers the range of operating parameters of interest to commercial production designers.

Each coil was tested in the following manner:

- The on coil air temperature was kept constant at $40\,^{\circ}\!C$
- The inlet water temp was kept between $6\,^{\circ}\!C$ and $8\,^{\circ}\!C$
- Fan speed was varied to implement face velocities from 3m/s to $6m/s$
- Water flow rate was varied from $40l/min$ to $120l/min$

---

[3] As a result of the single water circuit, the water delta T was only between 2 and 4 degrees but this is still within the range of producing acceptable accurate experimental results and energy balance.

Once steady state conditions were obtained, the following parameters were measured for each combination of air and water flow rates:

- Air Temperature, both on and off coil
- Water Temperature, both inlet and outlet
- Air pressure drop
- Water pressure drop[4]

The coil capacity was calculated for both the air temperature heat exchange as well as the water temperature heat exchange. The average of these two values was used in further calculations. Next, the *LMTD* was calculated from the fluid temperature differences. Although the heat exchange is one of pure cross flow, no correction factors were used, since at the range of temperatures used, the correction factors were approximately unity. The quotient of Capacity and *LMTD* provided the "*UA*" value for each operating point. Finally, this *UA* value was normalised for each heat exchanger by dividing by the respective tube and fin surface area. This approach permits a comparison of the overall average *U* values, with respect to available airside heat transfer surface area.

Furthermore, the calculated *U* values can be considered scaled values of the airside heat transfer coefficient h_o. Assuming negligible variation in fin contact resistance, and arguing that for each water flow rate, the tube convection coefficient h_i, and the tube wall conduction resistance will be identical, a comparison of h_o is obtained. In this manner, the respective performance of each heat exchanger surface can be assessed on a comparative basis. As the initial testing of proposed prototypes was of an exploratory nature to begin with, this procedure of direct comparison proved to be efficient and practical.

---

[4] The water pressure drop was only recorded as a matter of fact, as most of the cores tested had the same number of tubes and therefore would be expected to have similar water pressure drops.

The dimensions of the various prototypes were kept essentially consistent with the standard heat exchanger face dimensions and flow depth in all cases. In this manner, a direct comparison of the performance with respect to a common heat exchanger volume could be achieved. To regulate this, the same inlet and outlet water manifolds were used for each prototype tested, effectively fixing the face dimensions and coil depth. Also, in order to retain manufacturing integrity, the fabrication of the prototypes was carried out using standard tubes and components wherever possible.

Using the approach, described above, sufficient data was collected for each prototype in order to gain relevant insight to those factors which dominate in the heat exchange process attributing to the performance of a particular prototype. Systematically, it was endeavoured to build up a succession of continually improving models.

5.4   Test Results

The range of graphs in Figure 5.4.1 summarise the results of the measured parameters in comparison with those of the standard commercially available heat exchanger cores.

In graph(a) the capacity comparison is plotted as a function of the water flow rate on a volumetric basis. This is useful to compare performance at similar operating conditions. Graph (b) is a comparison of the air pressure drop as a function of frontal air velocity. Graphs(c) and (d) are the corresponding UA and U values plotted as a function of the tube Reynolds Number in order to characterise the type of flow. The tube Reynolds number is characterised by the tube hydraulic diameter. The U values have been obtained by dividing each UA value by the respective coil overall external heat transfer surface area.

From graphs (a) and (b), it is clear that the capacity and the pressure drop of the TMHE is considerably lower than that of the standard coils. The capacity of the TMHE is on average between 37-46% lower than the standard coils, while the pressure drop has reduced by 50-70%. The comparison of UA values of the TMHE coil, depicted in graph(c), is similarly subdued. Logically the main reason for the poor performance is as a result of the low tube heat transfer surface area, and the absence of any secondary surface area.
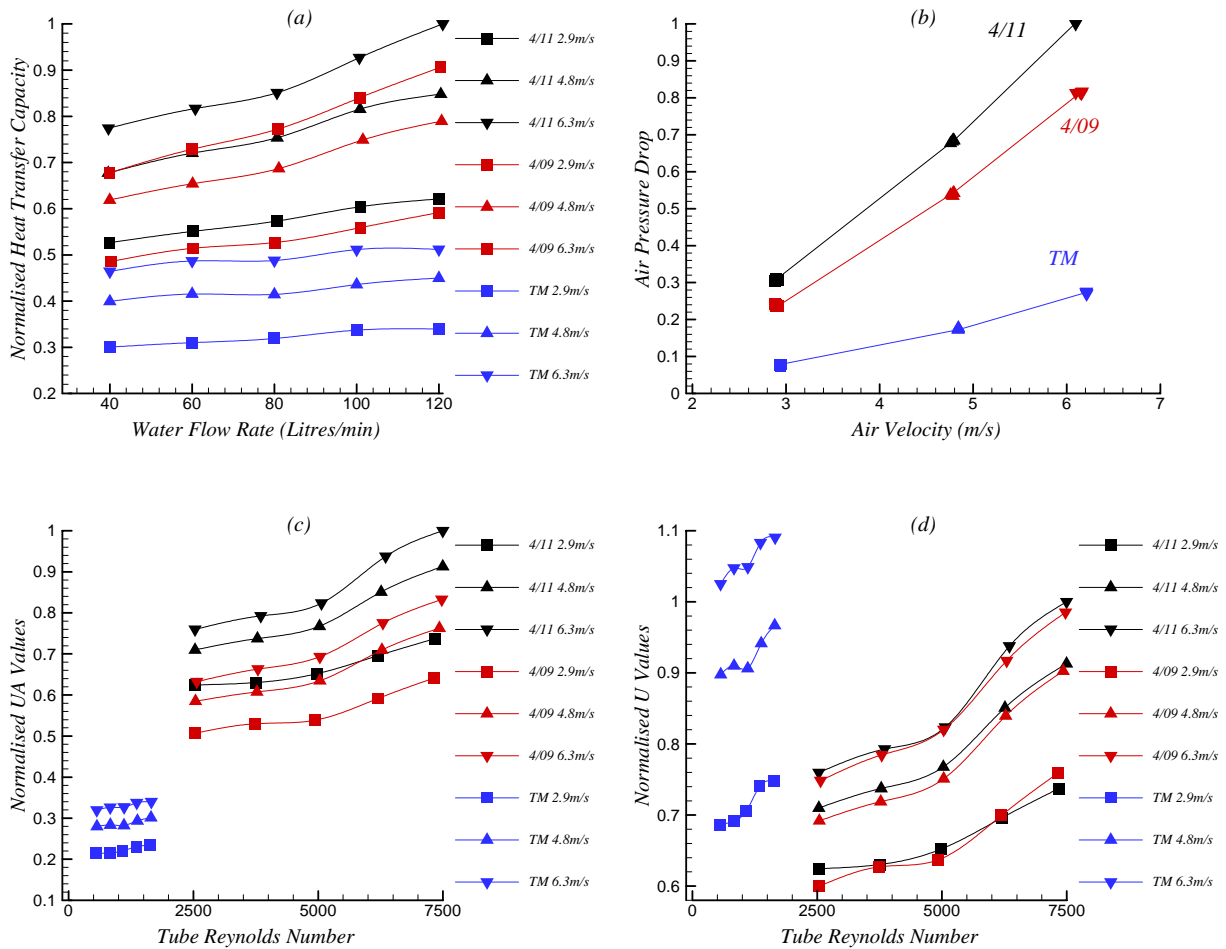
Figure 5.4.1 Performance comparison characteristics of the Tube Mesh coil versus the Louvre fin coils, at air velocities of 2.9,4.8 and 6.3m/s. The Tube mesh is operated with both horizontal and vertical tubes active. Note that the results have been normalised with respect to the maximum values occurring for the case of the 4row11fpi coil

The comparison of the normalised U values in graph(d), demonstrates the effectiveness of the TMHE as a heat transfer surface. The heat transfer surface area of the TMHE coil comprises solely of the external tube area calculated to be $3.17m^2$. For the standard coils the fin area was included, and was calculated to be $10.85m^2$ and $9.15m^2$ for the 11fpi and the 9fpi coils, respectively. The TMHE coil has a vastly superior U value to the two commercial coils. The U value of the louvre fin coil having $11fpi$ is marginally higher than the one having $9fpi$ although this difference is less obvious at lower air Reynolds Numbers. Thus the TMHE surface geometry has a higher average external convection coefficient than the standard tube fin arrangement. Clearly, commensurate with the predictions, there is increased turbulence and hence better fluid mixing. This is presumably brought about by the meandering flow path, and flow disturbance due to the tube obstacles. Due to the relatively large dimensions of the open mesh geometry the flow is not constrained between narrow channels as it would be in a confined channel. Therefore there is less "quenching" of any turbulence or vortex shedding that may be generated from the upstream vertical and horizontal tubes.

It is apparent that the two louvre fin coils have similar U values at all water and air flow rates. Thus the U value is independent of the fin pitch in this case. Logically the increase in capacity is obtained by the increase in fin surface area, although not in direct proportion. There is a 10% increase in capacity but this is due to the 18% increase in fin surface area. So although increasing fin density increases the surface area, it does so to the detriment of the average external convection coefficient, and the law of diminishing returns applies. As the fin spacing decreases, the Reynolds number decreases and excessive laminarisation of the flow results. The disproportionately higher pressure drop is evidently due to increased viscous drag, which tends to promote boundary layer growth and hence diminishes the convection coefficient. This reflection supports the merits of the open mesh heat transfer surface area concept. It also challenges the belief that fin spacing has negligible effect on heat transfer performance.

With respect to the lack of heat transfer performance of the tube mesh heat exchanger, another cause has been considered. It is possible that another reason for this lack of performance is that in the vertical tubes the water flow Reynolds Number

remains below 2000 at all flow rates. As a result the flow is laminar resulting in considerably lower internal convection coefficients. To establish how the lower tube convection coefficients may affect the overall heat transfer capacity, a comparison of the tube convection coefficients relative to the airside convection coefficient have been plotted in Figure 5.4.2. Although the internal convection coefficients are reduced due to the low water velocities they are still approximately 5 to 8 times that of the corresponding airside convection coefficients. Thus it remains that the overall U value is limited by the lower air side convection coefficient as is typically the case.
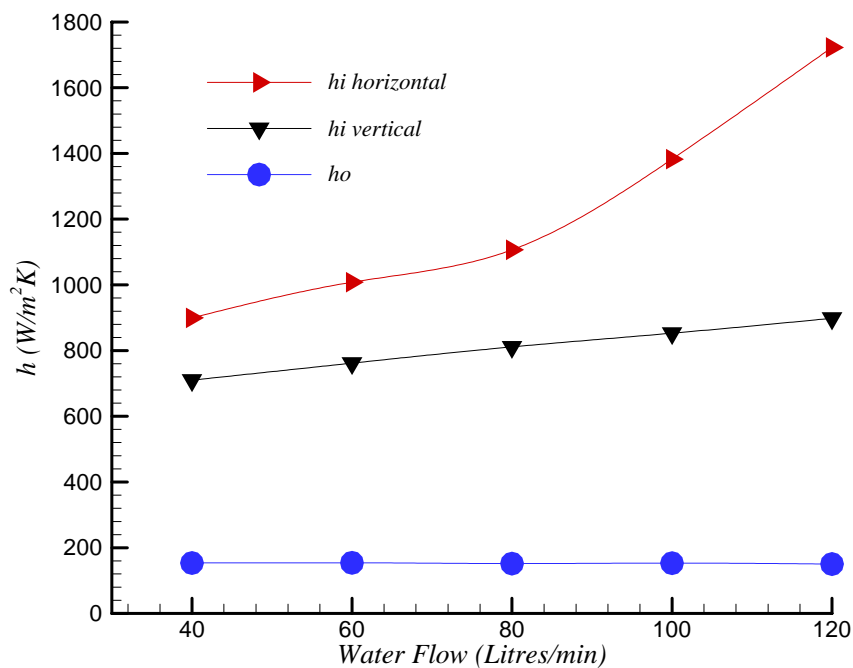
Figure 5.4.2 Comparison of vertical and horizontal tube internal convection coefficients as well as airside external convection coefficient at various water flow rates. It is assumed that the water flow is proportioned equally between the horizontal and vertical tubes

The heat exchanger was then tested by pumping the water through alternatively the horizontal tubes only, and then the vertical tubes only. This was done in order to establish the heat transfer contributions of each set of tubes. The next group of graphs in Figure 5.4.3 demonstrate the results obtained by testing the tube mesh heat exchanger with the water flow through alternately the horizontal and vertical directions.
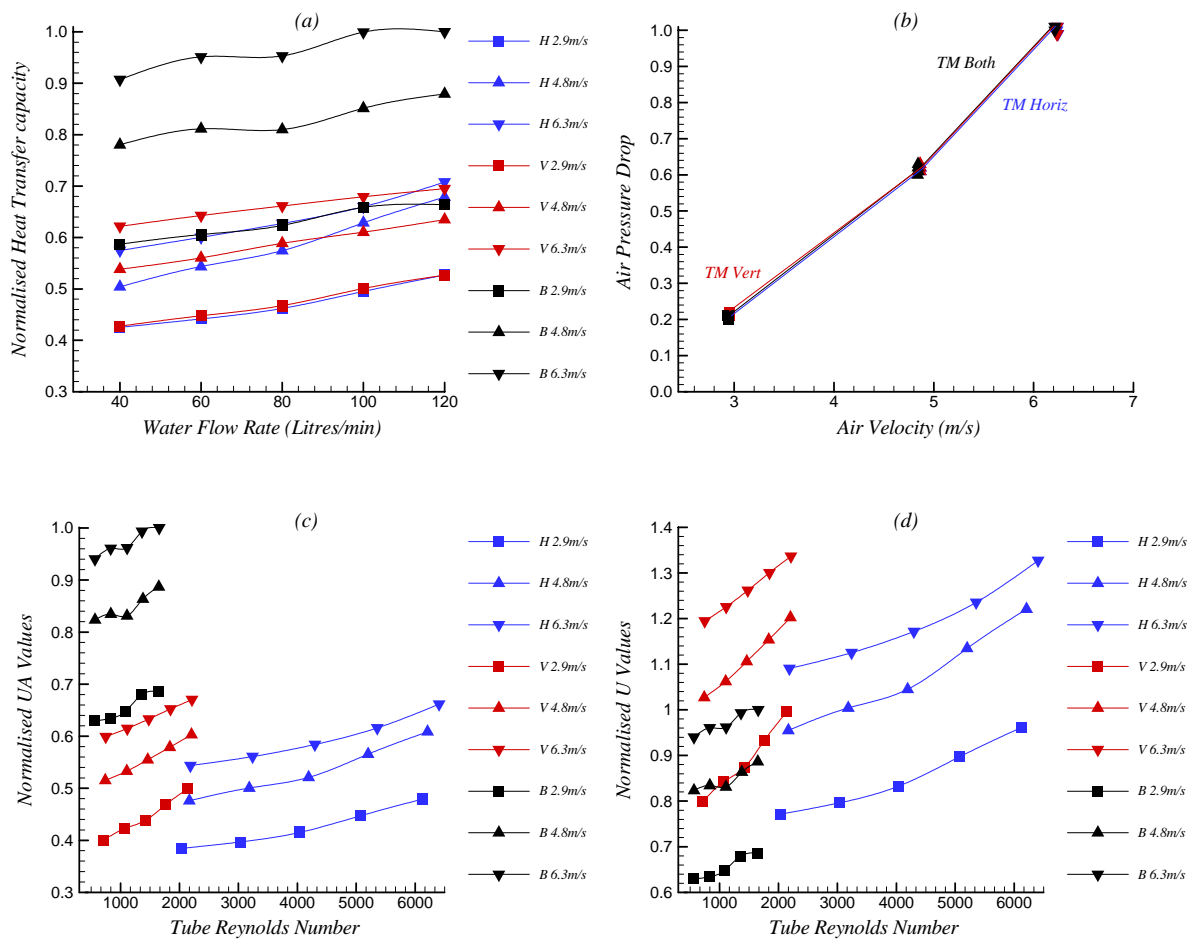
Figure 5.4.3 Performance comparison of the Tube Mesh coil when tested with both sets of tubes active, and then only the Horizontal , or Vertical tubes active. The air velocities are 2.9,4.8 and 6.3m/s. Note that the results are normalised with respect to the maximum values occurring for the case of both tube sets active

From Graph(a) the capacity of the TMHE with water flow in either individual direction is lower in both cases, comprising approximately 65%, of the capacity arising from that of flow in both directions simultaneously. This implies that the sum of the capacities for each flow direction is about 130% that of the capacity obtained from simultaneous flow. This shortfall in capacity in the case of the combined flow further verifies that, the associated lower internal convection coefficients are a limiting factor.

Also the capacity resulting from water flow in the vertical direction is marginally higher than in the horizontal direction. This is surprising because when flowing in the vertical direction due to the greater number of tubes the lower water velocities result in lower tube Reynolds numbers. Conversely however, the flow length is short and presumably the entrance lengths, are a substantial portion of the total length, thus accounting for enhanced heat transfer coefficients in this case. Depending on the tube inlet configuration, and water temperature, the hydrodynamic entrance length can be between 10 and 40 tube diameters, while the thermodynamic entrance length can be as great as 660 tube diameters[36]. It is therefore conceivable that the entry length can even equal the tube length in this case. Clearly, enhancing of heat transfer due to the tube entrance effects more than compensates for the reduction in Reynolds number.

As expected, Graph(b) demonstrates that the air pressure drop is similar irrespective of the water side utilisation.

In the horizontal water flow direction the tube Reynolds numbers are equivalent to the standard coils (graph (c)), and hence the internal convection coefficient cannot be the limiting factor. Rather, the lack of surface area is accountable for the low UA values in this case. In graph (d), these U values were obtained for the vertical and horizontal directions by dividing by the surface area of either the vertical or horizontal tubes respectively. This was justified on the basis that in either case, empty tubes do not actively contribute to heat transfer, even though they may affect the flow path and provide beneficial turbulence, ultimately improving heat transfer. This accounts for the U values for the horizontal and vertical directions being substantially higher than for the case of flow in both directions.
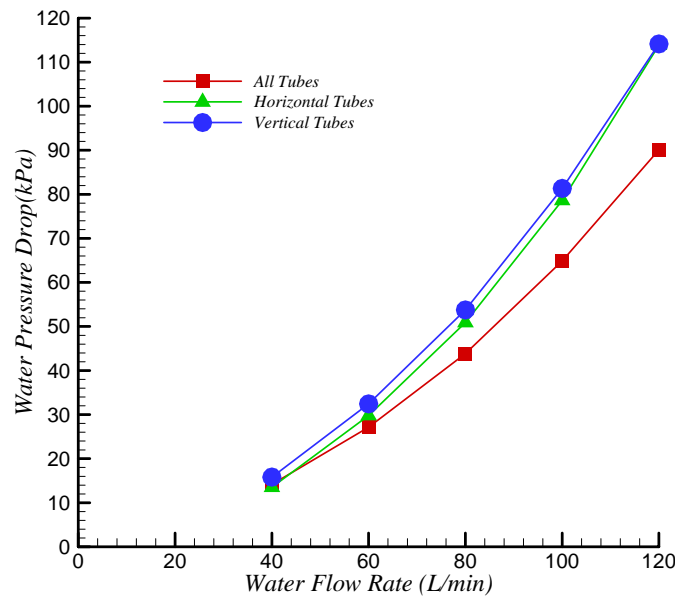
Figure 5.4.4 Comparison of tube water pressure drop when tested through alternating flow directions

In order to establish why the performance of the coil when tested in either the horizontal or vertical flow modes was similar, it is necessary to look at the water flow balance between horizontal and vertical directions. In the absence of any flow balancing devices, such as valves or the like, the measured waterside pressure drop in each case should provide an indication of the flow proportioning. Since there are many more tubes in the vertical direction, and they are shorter with less friction, one would expect there to be a greater proportion of the flow in this direction. However, as can be seen from Figure 5.4.4, the water pressure drop when either the horizontal tubes, or alternatively the vertical tubes are active, is similar at every flow rate. One can deduce that this purely coincidental, and an implication of this particular coils geometry. It would appear that the entrance effects of the numerous vertical tubes account for a large proportion of the overall pressure drop, which coincidentally balances that due to the longer but fewer horizontal tubes.

The air side heat transfer coefficient h_o was calculated at the various air velocities for the case of both sets of tubes active which demonstrated the highest performance. These results are compared with the results of the two louvre fin surfaces in Figure 5.4.5. Note that in order to calculate the air side heat transfer coefficient of the Tube

Mesh heat exchanger operated with both sets of tubes active, requires a variation of the overall thermal resistance equation. This is because the heat flow follows a parallel path through the horizontal or vertical tubes simultaneously. In addition the internal convection coefficient h_i is different due to the variation in tube velocity in either the vertical or horizontal tubes. Therefore in this case the airside heat transfer coefficient is given by,

$$h_o = (\frac{1}{U} - \frac{A_o}{h_{iv}A_{iv} + h_{ih}A_{ih}} - \frac{\delta_w A_o}{k_w A_w})^{-1} \qquad (1.1)$$

where the subscripts *iv* and *ih* refer to the vertical tubes and the horizontal tubes respectively.
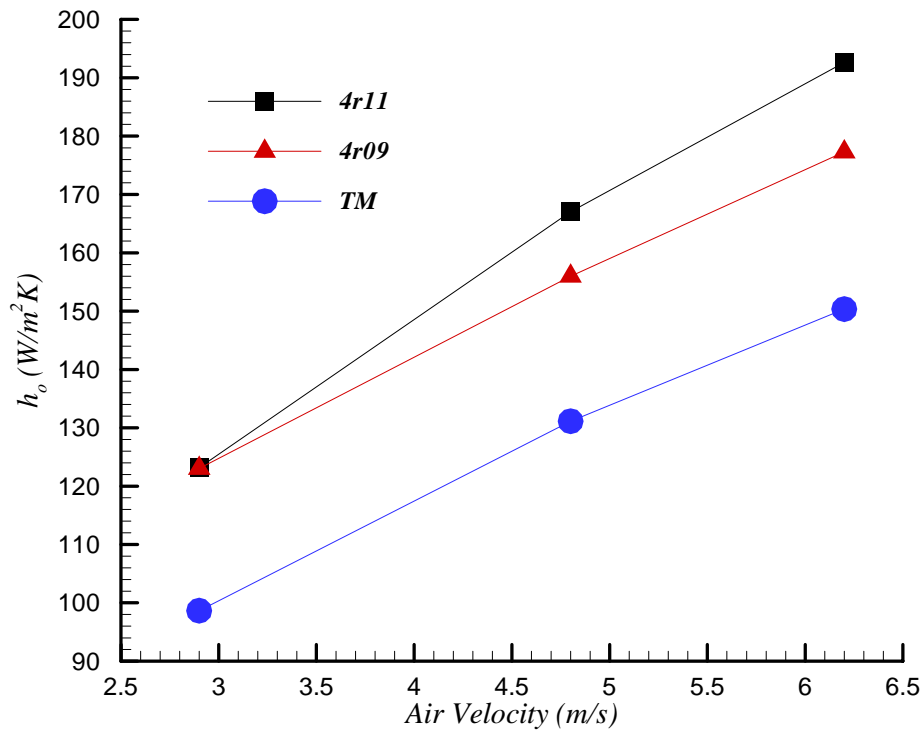
Figure 5.4.5 Air side heat transfer coefficient h_o comparison of the louvre fin surfaces and the TMHE with both sets of tubes active

The airside heat transfer coefficient of the tube mesh heat exchanger is considerably lower between about 80-85% of that of the two louvre fin surfaces. This result suggests that homogeneous turbulence does not substantially enhance heat transfer in a heat exchanger configuration. There are two possible reasons for this. Firstly, it is certain that the homogeneous turbulence levels are only established after some progression through the coil length and thus do not have any effect on the first several tube rows. The fluid flow at entry to the heat exchanger is still developing and the large boundary layers provide the resistance to heat transfer. It is at this location where increased turbulence would be most beneficial, assuming that there is sufficient kinetic energy to disrupt or minimise boundary layer thickness. It is possible that the turbulence levels are not high enough to adequately disrupt the boundary layers. Secondly by definition homogeneous turbulence is not predisposed towards fluid conveyance like other forms of turbulence. Even if the turbulence intensity levels are high enough to disrupt the boundary layers, fluid transport and exchange at the tube surface is required to facilitate heat transfer. The random oscillating character of the flow remains contained to a local position within the bulk flow and hence does not transport fluid across large distances. In other words the convective capability of homogeneous turbulence is minimal.

The pin fin heat exchanger on the other hand has locations where specific vortices are generated. These transverse or stream wise vortices are more effective in energy transport than homogeneous turbulence.

5.5   Conclusion

In general, the Tube Mesh coil has a lower heat transfer capacity than the two louvre fin coils when compared on a per unit volume capacity basis. This is undoubtedly due to the minimal tube surface area and the absence of any secondary heat transfer surfaces. However it has been demonstrated by comparing normalised U values that the TM geometry has a considerably higher overall heat transfer coefficient. This is due to the minimal heat transfer surface area. On the other hand due to the open mesh structure, the air pressure drop through the TMHE was extremely low in comparison to the tube-fin coils.

It was shown that although the tube velocities in both sets of tubes are low, and in most cases the flow remains laminar, this does not diminish the waterside convection coefficients enough to make them a limiting factor.

Also, it was established by independently testing the two flow directions, that the capacity and the pressure drop were similar for either water flow direction. Therefore, with regard to water flow rate, this particular coil is naturally balanced. This implies that the capacity of the TMHE is at its optimum operating capability, and little would be achieved by biasing the flow in either the horizontal or vertical direction.

It was found that the air side heat transfer coefficient of the TMHE was lower than the louvre fin coils by approximately 20%. It was suggested that one reason for this was that the final turbulence levels may not be established early enough during the course of the fluid through the mesh of tubes. Hence the first tube rows do not benefit from any increase in turbulence levels where they would be most beneficial. In addition it was surmised that homogeneous turbulence by definition has minimal convective attributes, since it does not facilitate a high degree of secondary fluid transport. Thus in spite of the open mesh, unless specific convective type flow structures are established, minimal convective enhancement can occur.

Chapter 6

Effect of Transverse Vortex Structures combined with Leading Edges

6.1   Introduction

It was established in the previous chapter that homogeneous turbulence generated by the heat exchanger surface does not adequately enhance the air side heat transfer coefficient. This chapter aims to investigate the effect of transverse vortex shedding from parallel plate arrays combined with the heat exchanger tubes. The parallel plate arrays are designed to generate transverse vortices, and provide multiple leading edges. As reported in Chapter 2, a review of the literature had revealed the promising flow characteristics, with respect to vortex generation and increased heat transfer, of so called parallel plate arrays. Parallel plate arrays have been studied quite extensively by various researchers like Yun and Lee[70],Wang et al[37] and Dejong and Jacobi[7]. They found that when a fluid flow was introduced to a suitably arranged array of plates, at a particular Reynolds number, vortex shedding was seen to occur towards the rear of the array. As the Reynolds number was increased, the point of initiation of the vortex shedding shifted upstream towards the entrance of the array. The vortex shedding led to an increase in heat transfer, with a minimal increase in pressure drop. Of course the numerous leading edges also contributed significantly to the increased heat transfer. Of more practical significance, their application with respect to heat exchangers can be found in the slit fins or the offset strip fin surfaces as reported in sections 2.2.2.3. With regards to the current series of investigations, the possibility of replacing the vertical tubes in the foregoing tube mesh heat exchanger with thick conducting struts that collectively would resemble a parallel plate array was investigated. Moreover the conducting struts would ideally intersect with the tubes so that they perform as thick fins, facilitating conduction, thereby increasing the surface

area of the tubes. Of course the resulting flow field would be much more complex than a typical parallel plate array due to the presence of the tubes.

The intention was to arrange the struts in a staggered array, and compare the heat transfer and pressure drop performance with the tube mesh heat exchanger as well as the louvre fin coils. It is understood that the level of transverse vortex shedding is highly dependent on the parallel plate array geometry. The plate thickness and spacing are the significant variables in this type of geometry. Thus the effect of various strut spacings and strut thicknesses would be compared in order to observe if any trends could be established. Three prototypes were fabricated, the second and third prototypes having double and triple the number of struts respectively. In order to accommodate the increase in the quantity of struts, without restricting free flow area substantially, these struts were cut from progressively thinner sheeting as described below. The performance of the three prototypes was evaluated on the heat and mass flow rig. In order to compare the measured performances against the characteristics of the fluid flow, a flow visualisation study was performed. It was speculated that although the flow structure would undoubtedly be complex due to the intersection of tubes and struts, the shedding of vortices may still be dominant. The effect of inhibiting any three dimensional structure due to viscous damping by the narrower strut spacing could be visualised.

In addition, another option for increasing the secondary heat transfer surface, while maintaining the same number of struts, is to increase the width or "chord length" of the struts. Of course increasing the chord length leads to overlapping of the struts, and this may introduce other limiting factors. The effect of this parameter was not evaluated experimentally, since it would require many additional prototypes. Therefore, a CFD comparison was performed in order to determine the effect of increasing the chord length, and this was extended to include the three strut spacings.

6.2 Flow Visualisation Comparison

6.2.1 Model Description

Three Perspex models were fabricated for the visualisation performed in the water tunnel using a dye visualisation technique. Photographs of the Perspex models are shown in Figure 6.2.1. The perspex models were a three times scaled up version of a section of a conventional tube fin radiator core having 4 rows of tubes. The tubes were cut from 8mm thick perspex sheet and mounted on a perspex base. The struts were cut from 1.5mm perspex sheet and were slotted on both sides at intervals corresponding to the transverse tube pitch. Corresponding grooves were milled into the tube flats, at one of three pitches thus facilitating the three strut spacings. By inserting the struts into the corresponding tube slots, the three models with various strut spacings on similar tube bundles were assembled.

Sp=P$_t$ Sp=P$_t$/2   Sp=P$_t$/3
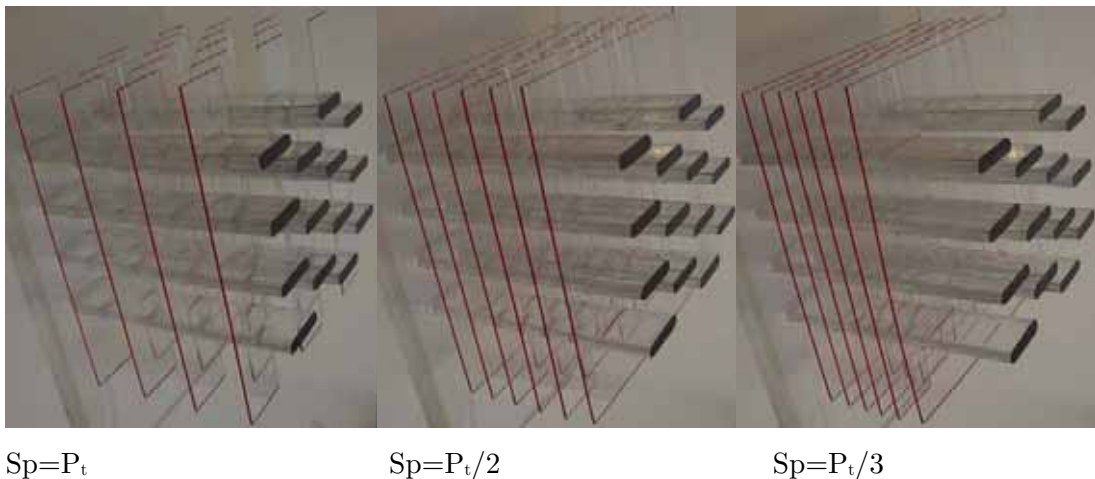
Figure 6.2.1 Photographs of the Tube Strut Perspex flow visualisation models

If the tube pitch is given by P$_t$, then the strut spacing was given by $S_P = P_t$, $P_t/2$ and $P_t/3$ in each case. Note that in each case the strut thickness t was kept constant and is given by $P_t/t = 24$. Each model had either 6 or 4 rows of struts in the first row, and also because of the difference in strut spacings, the models had varying widths. And, apart from the prototype with maximum strut spacing (ie $S_P = P_t$) the struts did not span the entire cross section of the water tunnel. Thus in order to prevent excessive flow bypass, and ensure a uniform flow velocity onto each model, it was necessary to include baffles attached to the rear of each model. Similarly the height of the models
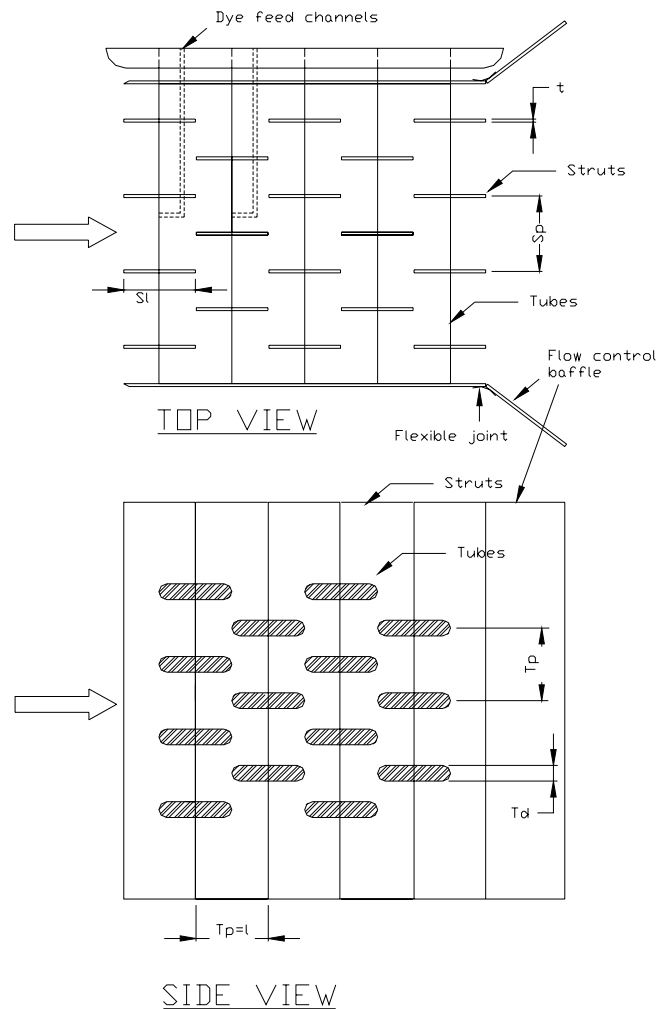
Figure 6.2.2 Sketch of the Perspex model construction of the Tube Strut prototypes

was less than the depth of the tunnel, and another baffle was attached to the bottom rear of the models to control flow bypassing underneath the model. By adjusting the three respective baffles at each water flow velocity, it was possible to ensure a uniform velocity profile entering the front of each model. The arrangement of the models and flow control baffles is illustrated in Figure 6.2.2.

In order to introduce the dye in the least obtrusive manner, the dye was released from the tube surface stagnation point. In order to facilitate this, a 1.5mm shaft was drilled into the tube stagnation point at an axial location midway between the front centre

strut and the next downstream strut[1]. Another shaft was drilled from the perspex backing plate, along the axis of the tube to intersect with the first shaft. The resulting channel allowed dye to be introduced at the tube end, so that it emerged from the tube stagnation point. The two centre tubes in the first tube row, and the centre tube in the second row were adapted in this manner. This allowed the simultaneous feed of three different coloured dyes to the model, without resulting in any downstream turbulence commonly associated with a dye probe. The dye feed channels can be seen in the sketch of Figure 6.2.2.

6.2.2   Procedure

The water tunnel was calibrated for the three water velocities of interest as described in Chapter 3. The models were tested with water flow speeds corresponding to Reynolds numbers equal to 2600, 3400 and 4600 respectively, based on a length dimension equal to the tube pitch P_t. At each velocity setting, the two side baffles, as well as the bottom flow control baffles were adjusted until the approaching fluid flow was uniform in both the horizontal and vertical direction. In order to verify this, a hydrogen bubble generator wire with corrugations was mounted some distance upstream from the model. The resulting parallel bubble streaks provided a distinct dynamic representation of the velocity profile approaching the model. Once a uniform approach velocity profile was established, the hydrogen bubble generator wire was removed. Red, blue and green food dye was used for the visualisation. A digital video camera was used to capture approximately 1 minute of footage at a frame rate of 25fps for each flow condition.

6.2.3   Results

The following collage of photographs represents a select sample of the video footage, and provides a summary of the resulting flow characteristics for each test. Note that the images are grouped by their respective Reynolds numbers for comparison. The water flow is from left to right in all cases.

In Figure 6.2.3, the results of the visualisation are compared for the case of Reynolds number equal to 2600.

---

[1] Locating the dye exit points in this location provided a clear line of site flow path between the struts. Thus any dye impingement onto the struts is due to transverse fluid motion.
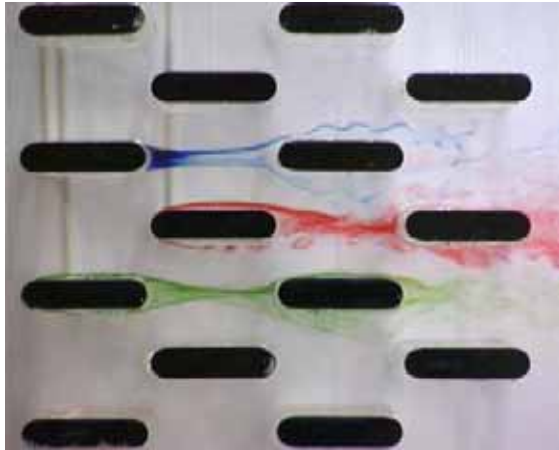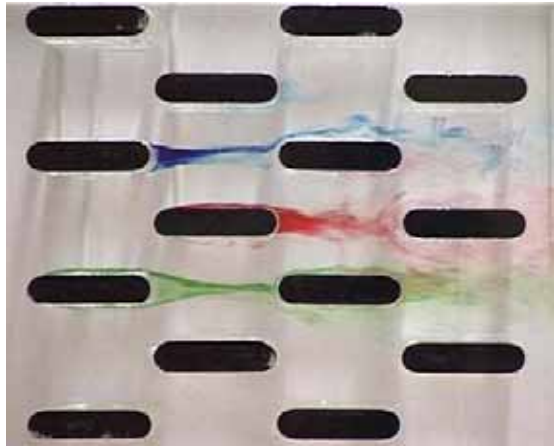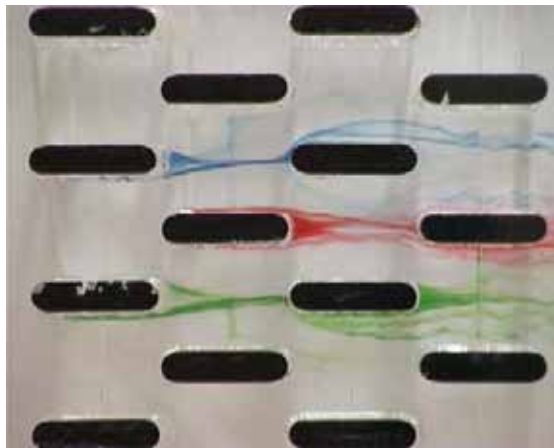
a)Side view for Sp=P_t
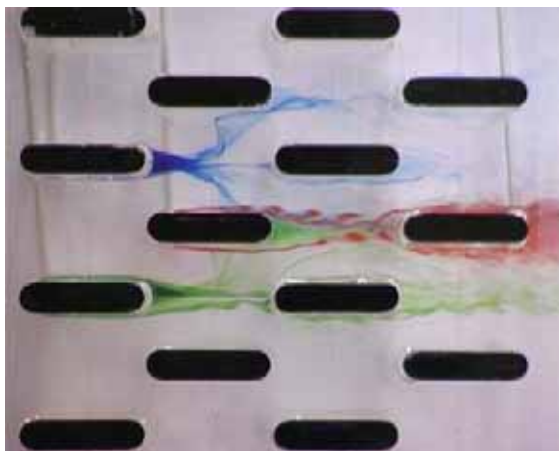
b)Side view for Sp=$P_t/2$
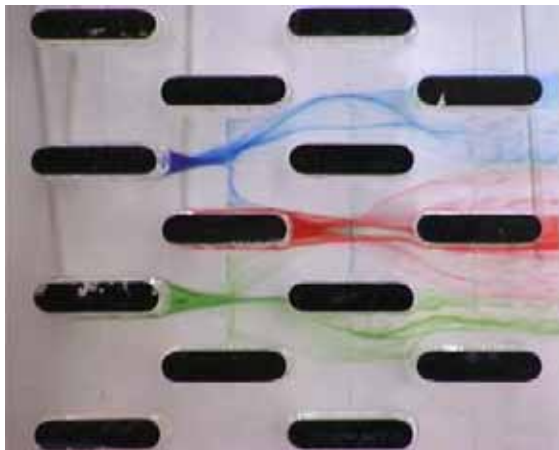
c)Side view for Sp=$P_t/3$

Figure 6.2.3 Flow visualisation results of the Tube Strut HE at a flow velocity corresponding to Re=2600

At the largest strut spacing equivalent to the tube pitch shown in Figure(a), it can be seen that the boundary layers around the first two rows of tubes are laminar. Flow instabilities occur at the rear of the third tube row, and by the 4th row, the boundary layer is completely disrupted giving way to large scale turbulence.

In the case of medium strut spacing Figure (b), the boundary layers over the first two rows are still laminar, but there is evidence of transverse fluid motion probably initiated by wake effects of the first row of struts.

Due to the narrower strut spacing this transverse fluid motion impinges on the struts and this leads to vortex shedding at the leading edges of the third row struts. The shed vortices persist in the wake of the second tube row until impinging on the 4th tube row. The blue dye impinging on the struts, gives the following tube a wide berth indicating that there is a large stagnant zone at the tube/strut interface. At the narrowest strut spacing Figure (c), the presence of the struts is clearly restricting any transverse fluid motion in the wakes of the tubes. The dye is impinging on the leading edges of the struts, and then bypasses the stagnant zones at the
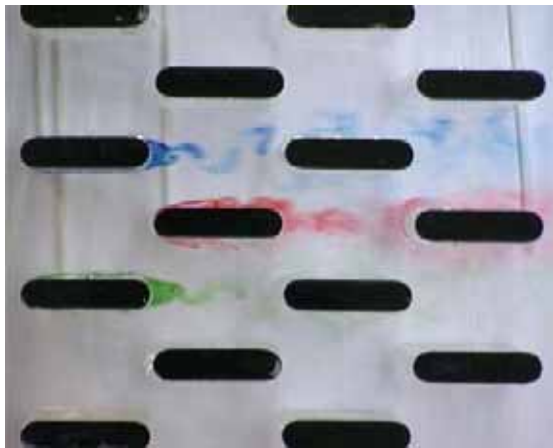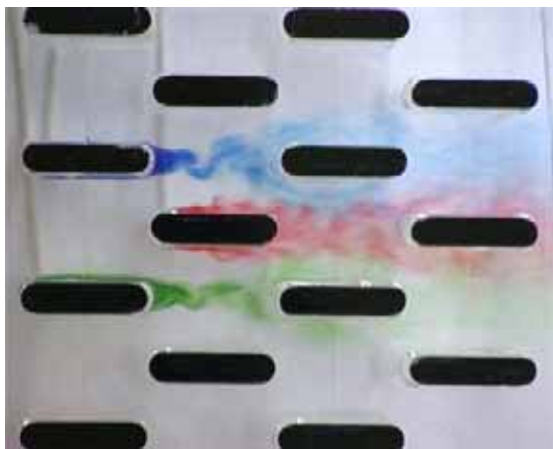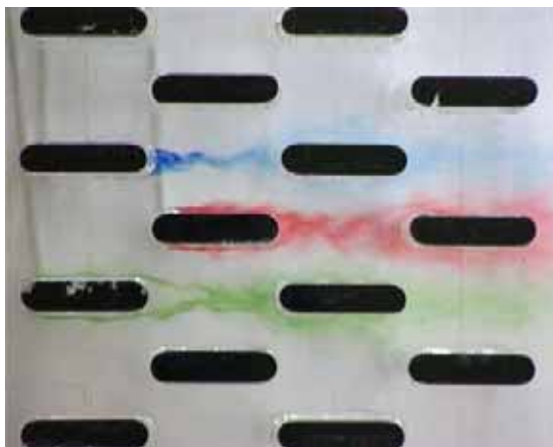
(a) Sp=P_t

(b) Sp=P_t/2

(c) Sp=P_t/3

Figure 6.2.4 Flow visualisation results of the Tube Strut HE at a flow velocity corresponding to Re=3400

tube/strut interfaces. There are two streak lines over the 3rd tube row. One streak line is closer to the tube profile, and is due to fluid which is moving in the centre space between the struts, and bypasses the tube at the stagnation point due to the thinner boundary layer around the tube. The other streak line over the 3rd row is further from the tube profile, and due to some dye following a transverse path until it impinges on the strut leading edge, it adheres to the strut and then is caused to divert broadly around the thicker boundary layer at the tube strut intersection. The flow is much more suppressed and laminar in appearance than the previous wider strut spacings. However, there is a suggestion of very weak vortex shedding at the intersection of strut and 4th tube row.

In Figure 6.2.4 the three strut spacings are compared at a Reynolds number of 3400. In Figure (a) at the widest spacing, the flow features are similar to that of the Re=2600, but with slightly more energy and slightly larger turbulent structures.

(a) Sp=P_t

(b) Sp=$P_t/2$

(c) Sp=$P_t/3$

Figure 6.2.5 Flow visualisation results of the Tube Strut HE at a flow velocity corresponding to Re=4600

The region of onset of flow instability has shifted upstream to the front of the 3rd tube row. At the middle strut spacing in Figure (b), there is definite vortex shedding occurring in the wake zones of the first tube row and are present over the second tube row. Also the boundary layers are small and clearly unstable. At the narrow strut spacing in (fig. c) the stream wise vortices have been surpassed by the close strut spacing. The boundary layers over the 3rd row are much larger than for the preceeding case and the flow appears laminar.

In Figure 6.2.5 the three strut spacings are compared at a Reynolds number of 4600. In Figure (a) at the widest strut spacing there are distinctive von Kármán vortices shed from the wakes of the first tube row. This surprising result can be explained by noting that if one recalculates the Reynolds number based on the tube depth, rather than the tube pitch, the Reynolds number is 980. This is within the expected range of von Kármán vortex generation. The presence of the von Kármán vortices implies that the bulk flow channelling between the

struts is two dimensional in nature. Although a two dimensional flow is not desirable with respect to heat transfer, the large scale oscillations have alternative beneficial heat transfer effects. The shedding of von Kármán vortices are expected to eliminate any stagnant wake zones behind the 1st tube row, and hence improve heat transfer contribution from the 1st row. The oscillations resulting from the vortices downstream of the first row span almost the entire flow width between the tubes of the second row. They therefore influence and disrupt the boundary layers over the second tube row so that there are no von Kármán vortices shed from the second row. Similarly the vortices shed from the first row impinge directly on the third row disrupting the boundary layers around the tubes in this row, and also prevent the shedding of vortices from this row. In addition, the vortices impinging directly on the 3rd row and indirectly on the 2nd row thereby causing a disruption of the boundary layers around these rows could be expected to improve heat transfer contribution from these tube rows. By the 4th row, however, all of the vortices have dissipated into general homogeneous turbulence. At the medium strut spacing, Figure (b) there are also von Kármán vortices present but they seem to be more diffusive in nature than those present at the wider strut spacing. Clearly the fluid displacement effects resulting from the strut finite thickness causes a departure from the more two dimensional flow represented by the more typical von Kármán vortices shed at the wider strut spacing. This is seen to a greater degree in Figure (c) showing the narrowest strut spacing. There is a very slight indication of von Kármán vortices present and the street is much smaller in scale (less than the tube thickness) than the previous two cases. In general the flow is more subdued and clearly less turbulent than the previous two cases.

6.2.4 Discussion

From the observations made of the flow visualisation, some generalisations can be deduced. In the case of the widest strut spacing, the interaction of the struts with the bulk fluid flow is limited due to their sparse distribution. Therefore the bulk fluid flow appears to be two dimensional in nature, especially at the highest Reynolds number flows whereupon Von Karman vortices are shed. There is likely to be an improvement in local heat transfer due to the vortex shedding. At the middle strut spacing the influence of the struts on the bulk fluid flow is more obvious as demonstrated by the onset of vortex shedding even at the lowest Reynolds number. It is evident that

transverse fluid motion initiated by the displacement of fluid caused by the finite strut thickness of the first strut row, causes vortex shedding at the leading edge of the second strut row. As the strut spacing is reduced further, the influence of the struts on the bulk flow becomes restrictive and the flow tends to relaminarise as any transverse motion and vorticity is quenched. In each case however, as the Reynolds number is increased the inertia forces caused by acceleration around the tube profile dominates the flow structure and the flow becomes two dimensional in nature so that the influence of the struts is not as pronounced. Thus from these findings the strut spacing can be optimised in order to increase heat transfer. Considering the geometries tested, the widest strut spacing is too wide for the transverse fluid velocity to interact with the bulk fluid flow, while the narrowest strut spacing is too restrictive on any three dimensional flow, providing a diminishing effect. Therefore the middle strut spacing appears to have the optimum geometry to facilitate desirable turbulent characteristics.

This of course does not take into account the increase in heat transfer surface area due to the increase in the strut density. Unfortunately, increasing the strut density to increase surface area, and the quantity of leading edges, also has a quenching and re-laminarising effect on the general turbulence characteristics. Furthermore, it appears that the influence of the strut thickness is an important and perhaps essential contributor in initiating transverse fluid motion which then gives way to strong vortex shedding. Moreover it may be speculated that if the struts are thick enough, there may be the possibility of vortex shedding from either the strut leading edge, or trailing edge or both. Clearly thinner fins would not produce the same level of fluid displacement or vortex shedding. Unfortunately thick fins increase the pressure drop as well as material requirements and weight. Thus by virtue of their presence, a limiting value can be associated with their spacing, and this has a limiting effect on heat transfer.

6.2.5   Conclusion from Flow Visualisation

The results of the flow visualisation study show that the resultant flow field through the exchanger is a combination of influences from the tubes and the displacement of fluid due to the finite thickness of the struts. The influence of the struts is highly

dependent on the strut spacing. At the widest strut spacing, their influence is minimal, as the struts are located in relative isolation. In this case the flow structure behaves similar to that of a plain tube bank, and at higher Reynolds numbers Von Karman vortices are shed by the front rows of tubes. At the middle strut spacing the struts exert a combined influence on the bulk flow structure so that at a critical Reynolds number stream wise vortices are shed, which can be expected to improve heat transfer. However, as the Reynolds number is increased, the influence of the tube profile outweighs that of the struts and the flow resembles that of a plain tube bundle. At the narrowest strut spacing, the struts are so close together that because of mechanical blockage they tend to suppress any transverse fluid motion, the fluid flow is restricted to 2 dimensions and the flow remains laminar throughout.

These findings suggest that the strut spacing can be optimised with respect to increasing turbulence. They also suggest that the strut thickness is required in order to displace the fluid and initiate transverse fluid motion which can result in vortices being shed from downstream struts. However, increasing the strut thickness has other design consequences. These include an increase in pressure drop and component weight. Nevertheless the findings were encouraging and prompted the fabrication of actual prototypes based on the above tube/strut combination, at the three strut spacings.

6.3 Prototype Performance Evaluation

6.3.1 Prototype 1

Figure 6.3.1 is a sketch of the Tube Strut coil prototype. It is constructed by replacing the fins of a standard coil with thick metal struts which are inserted between each tube row at much wider spacings than would be used for a typical fin pitch.

The struts span between, and intersect the horizontal tubes at the required spacing, creating a tube and strut junction at each intersection. Each successive row of struts is offset from the first, so that when viewed from the top, the resulting staggered arrangement of struts forms a parallel plate array of struts which intersect with the tubes. This results in a flow path, which has repeatedly interrupted flow passages created by the successive entrance regions of both tubes and struts.
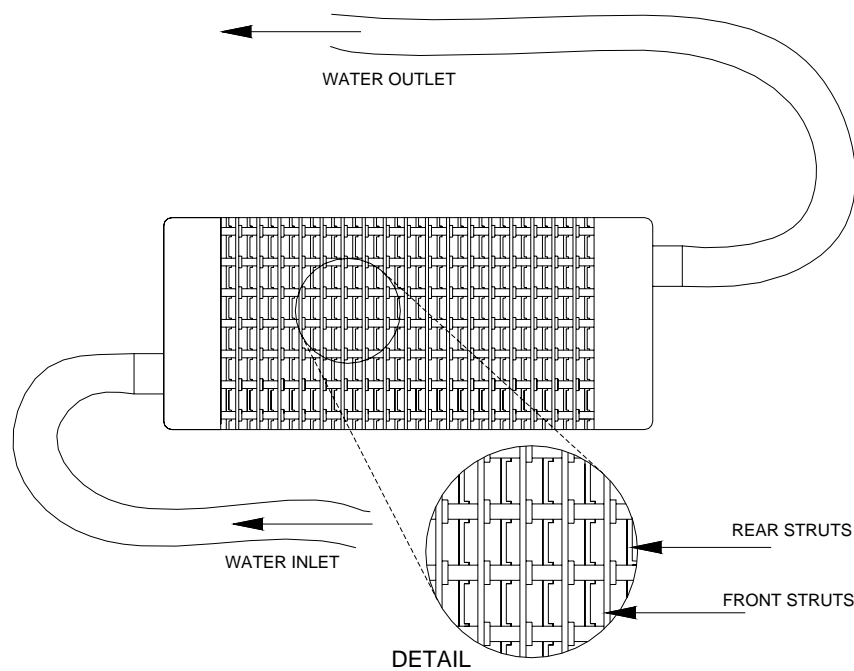
Figure 6.3.1 Sketch of the Tube Strut Heat Exchanger

The struts were fabricated by slicing existing coil manifold brass tube plate into strips. It was argued that the slight reduction of thermal conductivity of brass in comparison to copper would be insignificant considering the much thicker struts than typical copper fin sheeting. The brass tube plate is 1.2mm thick and has the tube holes pre-punched. The strips were sliced along each tube row centre line, as shown in Figure 6.3.2.
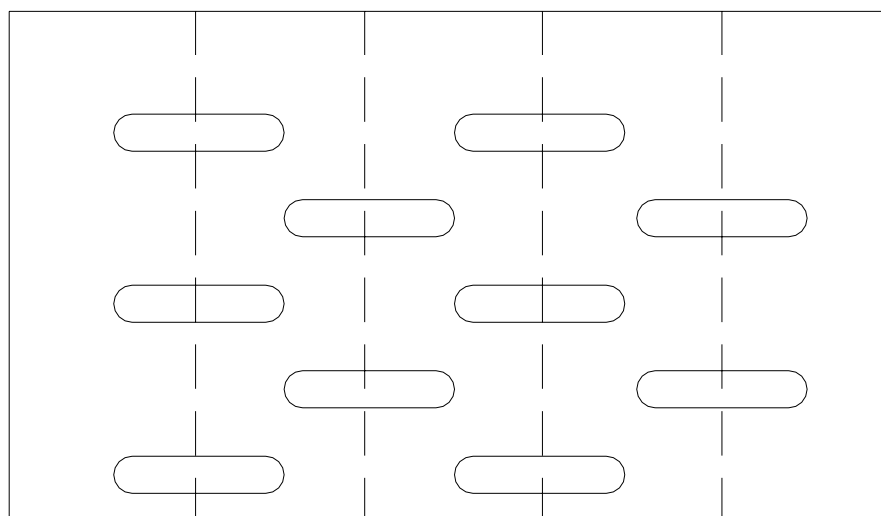

Figure 6.3.2 Sketch showing the positions of the Tube Plate cut lines

As a result of the punching process, there was a small flange around the perimeter of each punched hole. This provided a flat slot for the tubes to be supported upon. These struts were then slotted onto the tube bundle from one end and located at the respective design strut pitch Sp. In the case of Prototype 1, the struts were spaced at 12mm centres, which is approximately the same spacing as that of the vertical tube bundle used in the Tube Mesh heat exchanger. Therefore in comparison between the two, the inclusion of conduction at the tube and strut interface would be facilitated, without having to account for any difference in the quantity of vortex generators or leading edges.

At this point it may be useful to introduce an expression for the relative densities of the struts by virtue of an array parameter AP.

$$AP = \frac{Sp}{St}$$

Where Sp is the strut pitch, and St is the strut thickness. It is worth noting that the array formed in Prototoype 1 has an array parameter of 10 which is similar to the thin plate geometry evaluated by Dejong and Jacobi[7], which has an AP of 11.88. Conveniently, since the transverse tube pitch is approximately 12mm, the strut spacing Sp in this case is equal to the transverse tube pitch P_t, ie Sp=P_t.

The brass struts are approximately 12mm in width, which is wide enough to span between the centres of two adjacent tube rows. Thus the leading edge of each strut is located on the vertical centre line of the foregoing row of tubes and similarly the trailing edge of the strut is located on the following tube row along a vertical centre line. The arrangement is best envisaged by referring to Figure 6.3.3.

CROSS SECTION THROUGH AN ELEVATION

AIR FLOW

STRUTS   TUBES   TUBE HOLE FLANGE

AIR FLOW

CROSS SECTION THROUGH PLAN
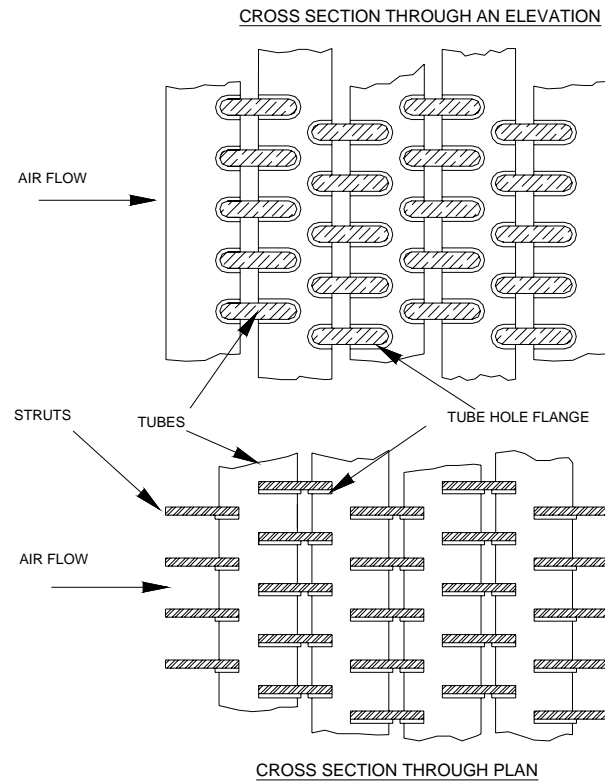
Figure 6.3.3 Schematic arrangement of the Tube Strut Heat Exchanger

Figure 6.3.4 is a close up photograph of a face view of the Tube Strut Heat Exchanger and gives an indication of the spacing and open arrangement of the conducting struts. 6.3.5Figure 6.3.5 is a plan view showing the strut arrangement.

The strut arrangement for this series of prototypes was assembled on the standard tube block of 74 tubes as used for the two commercial comparison coils having louvre fins of 11fpi and 9fpi fin densities. This obviates the need to determine the internal tube convection coefficients and tube conduction resistances, since these would be expected to be identical in each case.
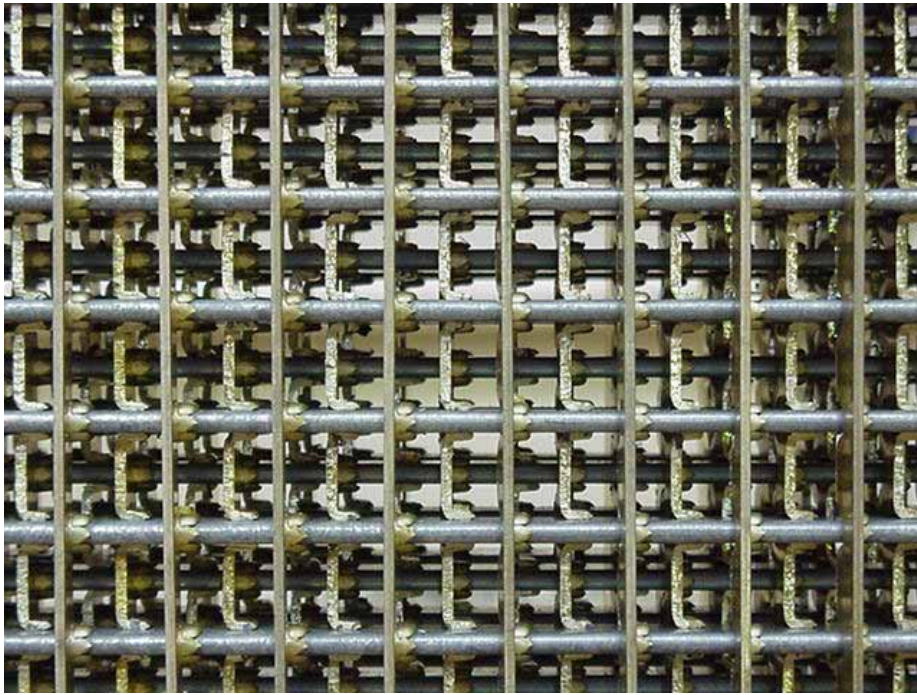
Figure 6.3.4 Close up view of the Tube Strut heat transfer surface, with $Sp=P_t$ and $St=1.2mm$
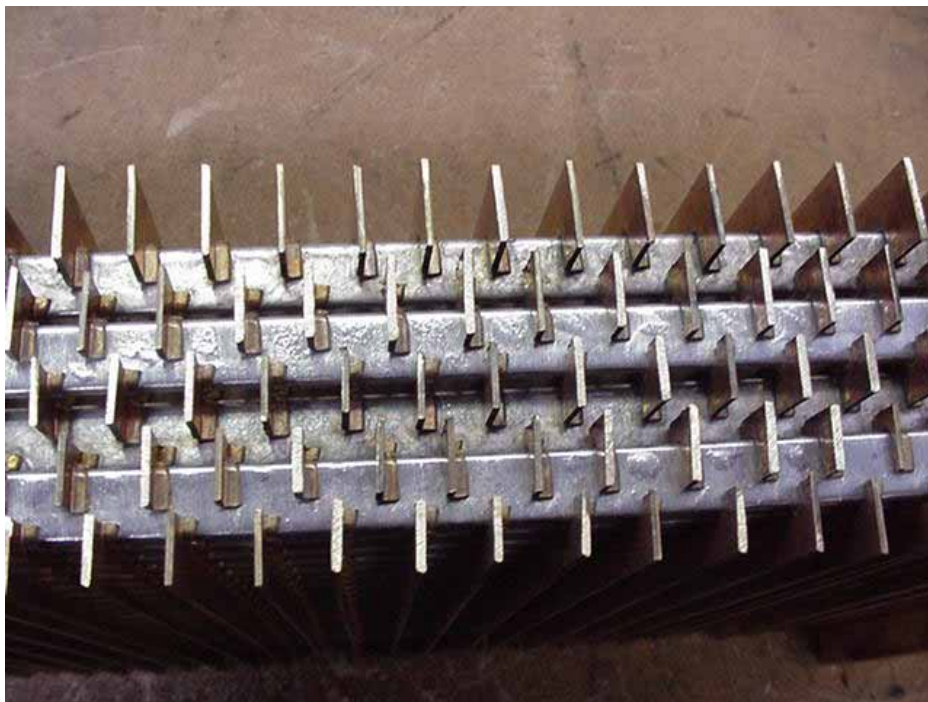
Figure 6.3.5 Top view of the Tube Strut Heat Exchanger

The Tube Strut heat exchanger is expected to exhibit the following advantages over conventional heat exchangers:

- The leading edge of the struts is located along the centre axis of each tube where the heat driving potential is at its highest.
- The thick struts have superior conductance to thin fins, which normally have high temperature gradients in the zones directly in front of the tubes, limiting their efficiency.
- Thick fins have less contact resistance than thin fins whose tube collars may distort during the tube insertion process.
- The wide spacing of the struts should allow the development and sustainability of horseshoe vortices at the tube/strut intersections, facilitating high Nusselt numbers at the front of the tubes.
- The absence of fin area in the wakes of alternate tubes, may reduce the wake area in these zones, improving heat transfer behind those tubes.
- The wide spacing of the struts for this prototype retains the open mesh theme and would result in low pressure losses.
- There would be less fouling potential, and the surfaces would be easier to clean.
- In dehumidifying applications, there would be less water carryover at high air velocities. Narrow fin spacing results in higher water carry over unless the face velocities are limited.
- In refrigeration applications, there would be less flow restriction due to frosting occurring on the heat transfer surfaces.
- The struts help to keep the tube assembly rigid.

6.3.2   Prototype 2

In the case of Prototype 2, shown in Figure 6.3.6, the struts were cut from 0.5mm copper sheet. In terms of fin thickness this can still be considered thick compared with the louvred fins which are 0.076mm thick. Also, this provided the same strut aspect ratio that was conveyed to the Perspex models used for the visualisation i.e. $P_t/24$. In fact the construction of Prototype 2 most accurately mimicked the construction of the

perspex model with a strut spacing having $S_p=P_t/2$. And since this model exhibited good three dimensional flow characteristics, good heat transfer capacities were expected.
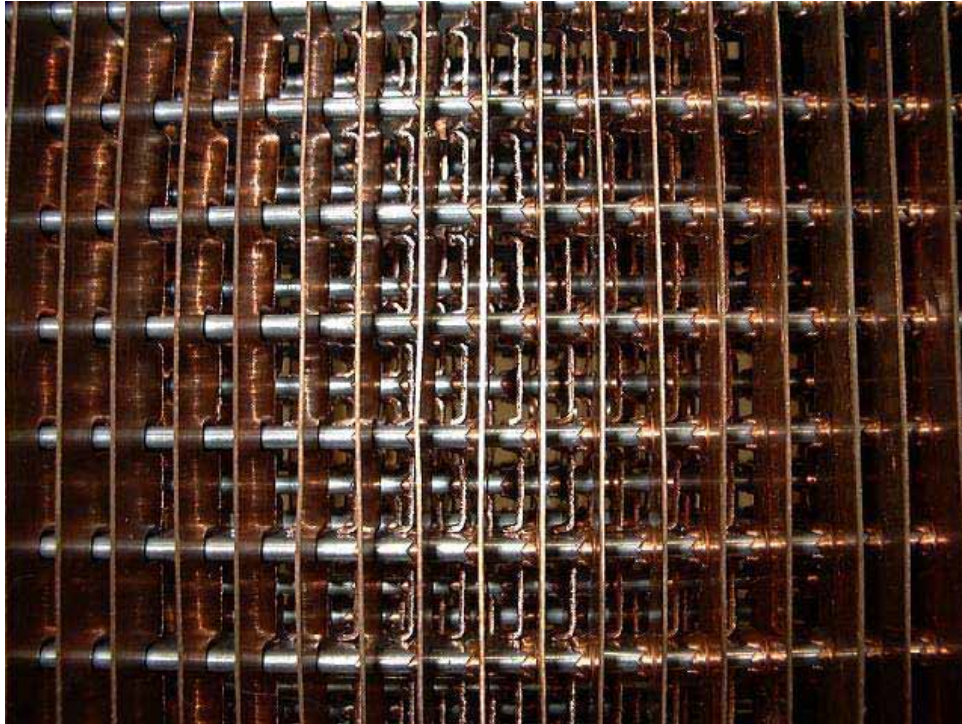

Figure 6.3.6 Close up view of the Tube strut heat transfer surface with $Sp=P_t/2$ and $St=0.5mm$

Prior to slicing the struts, the tube holes were punched into the copper sheeting in a similar manner to the manufacture of the brass tube plate. Apart from the difference in thickness the dimensions of the copper struts were the same as the brass struts used for Prototype 1. Since the copper struts were thinner the possibility existed that the contact between tube and strut may not have the same integrity as that of Prototype 1. The coil assembly was subsequently baked in a similar manner to the standard production process of the two commercial coils[2].

---

[2] The flat radiator tubes are seem welded from brass sheet and coated with a tin flux. During the baking process the flux melts and sweats into the fin and tube joints providing a thorough join minimizing the contact resistance.

6.3.3   Prototype 3

In this case the quantity of struts was triple that of the first prototype so that $Sp=P_t/3$ as shown in Figure 6.3.7.
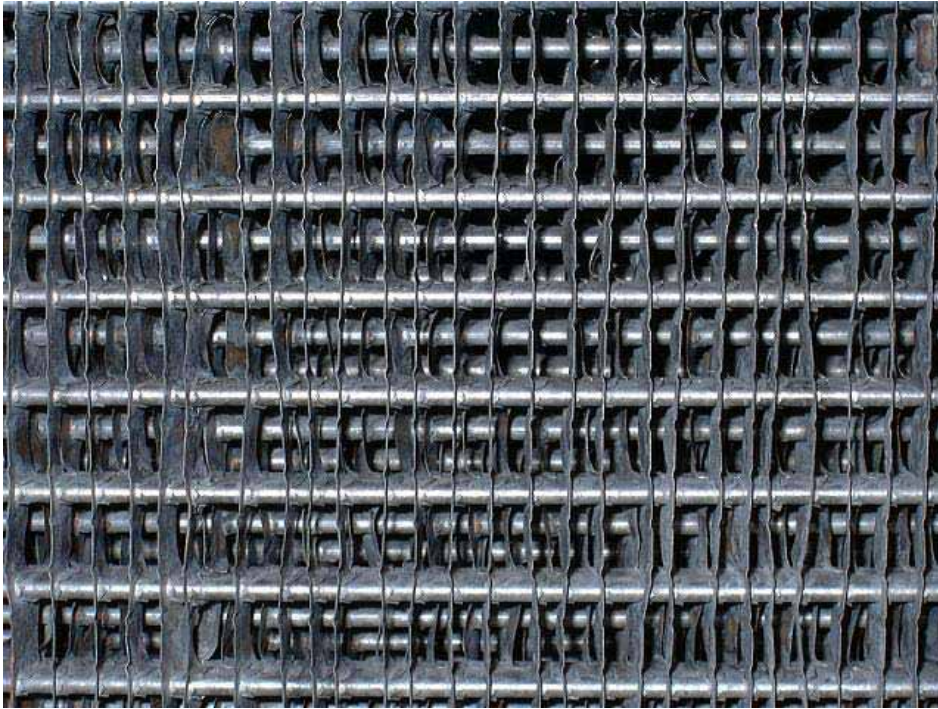
Figure 6.3.7 Close up view of the Tube Strut Heat Transfer surface having $Sp=P_t/3$ and St=0.076mm

This strut pitch is approximately 4mm, which is close to the fin pitch of the two louvre fin coils. Naturally this tends to diminish the open mesh theme to a certain extent. Therefore in order to limit pressure drop due to excessive blocking of the air path, the struts were cut from typical copper fin stock which in this case has a thickness of 0.076mm. Apart from this the coil construction was similar to that of Prototype 2, including the baking process. However because of the flimsiness of the struts and the manual fabrication process, a significant percentage of the struts were bent and mal-aligned causing a partial occlusion of the flow area. It was noted in a few cases that due to warping of the struts at the tube strut intersection, the contact at these intersections would certainly be compromised. Table.6.1 provides a specification summary of the construction parameters of each of the test coils.

Table.6.1 Specification summary of the test coils

Coil	Fin material	Fin thickness	Fin width	Fin pitch	Array Parameter
(Units)		(mm)	(mm)	(fpi)	AP
4row11	Copper	0.076	58	11	NA
4row09	Copper	0.076	58	9	NA
PT 1	Brass	1.2	12.2	2.08	10
PT 2	Copper	0.5	12.2	4.16	12
PT 3	Copper	0.076	12.2	6.24	82.11

6.4   Procedure

A detailed description of the closed loop test facility as well as the general procedure can be found in Chapter 3. Nevertheless, a brief summary of the test parameters with specific reference to this particular set of coil tests is repeated here.

- The test coils were each evaluated at three air inlet velocities of 2.9m/s, 4.8m/s and 6.3m/s.
- The air dry bulb temperature set point was maintained at 40 degrees Celsius at all times.
- The chilled water flow rate was varied between 40*l/min* and 120*l/min.* This resulted in corresponding Tube Reynolds numbers of between 2500 and 7200 approximately.
- The supply chilled water temperature set point was maintained at 11.5 degrees Celsius.

The chilled water set point temp was in the range of the minimum practical set point for the refrigeration circuit. This provided sufficient cooling capacity to match the heat transfer capacity of the 4 row 11 fpi commercial coil at the given inlet conditions. For a particular air inlet velocity which was then kept constant, the chilled water flow rate was adjusted from the minimum value, and incremented after each set of readings was finalised. Before each set of readings was taken the off coil air and water temperatures were permitted to reach steady state conditions and maintained for a period of 20 minutes.

6.5   Results

The first comparison that can be made is the difference in performance between the Tube Mesh heat exchanger tested in the previous chapter, and the so called Strut Mesh which has a strut spacing equal to the transverse tube pitch i.e. $Sp=T_p$. Note that for this comparison, only the horizontal tubes of the Tube mesh heat exchanger were active, and therefore the vertical tubes (now empty) can only contribute to turbulence generation. Recall that the vertical tubes had a spacing that is equal to the transverse tube pitch of the horizontal tubes, and therefore have a similar spacing to the strut spacing of the Tube Strut heat exchanger which is also equal to the transverse tube pitch. The graphs in Figure 6.5.1 show the comparison in performance between these two heat exchangers.

As can be seen from this set of graphs, the capacity of PT 1 over the Tube Mesh has increased significantly, and has virtually double the heat transfer capacity at all water and air flow rates. On the other hand the pressure drop of PT 1 has also increased. However this increase is only about a 50% increase, and is consistent at all flow rates.

Similarly the *UA* values of PT 1 have increased over the Tube Mesh coil by about 70%, and the normalised U values have increased by about 60%. In general there is a dramatic improvement in coil performance of PT 1 over the Tube Mesh. This clearly demonstrates that attempting to increase the turbulence levels without providing any secondary heat transfer area has no advantages. However, by providing a secondary heat transfer surface area in such a way that it contributes to the increase in turbulence, with limited pressure drop is preferential. However PT 1 has a shortfall in capacity compared to the 4row11 commercial coil by about 40%.

The following series of plots comprising Figure 6.5.2, Figure 6.5.3 and Figure 6.5.4 have all been plotted as normalised values with respect to the values obtained for the 11fpi coil which has the highest capacity at a water flow rate of 120l/min and an air velocity of 6.3m/s.
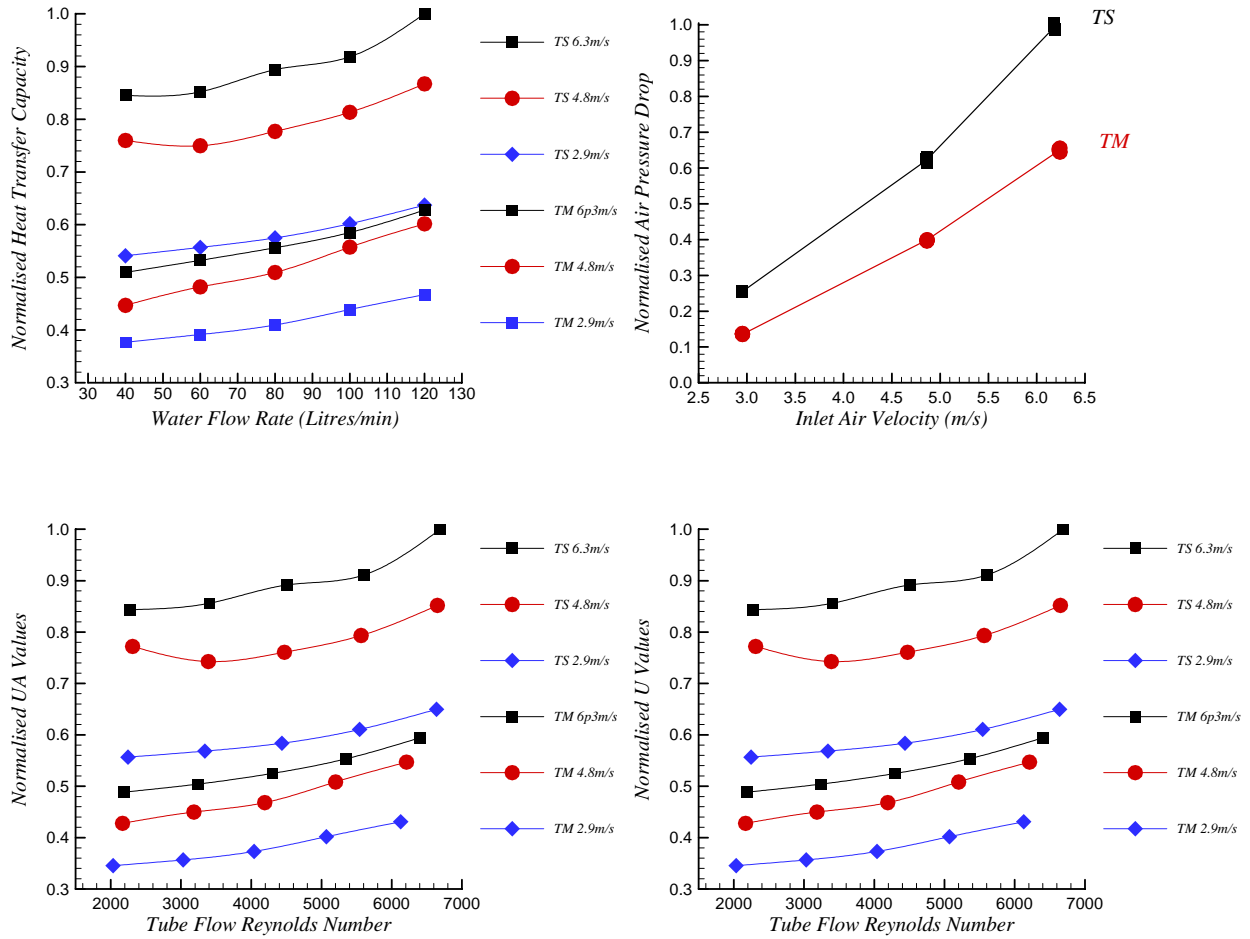
Figure 6.5.1 Performance comparison between the Tube Mesh and Tube Strut (Sp=Tp) heat exchangers at air velocities of 2.9,4.8 and 6.3m/s. The results have been normalised with respect to the maximum values occurring for the Tube Strut heat exchanger
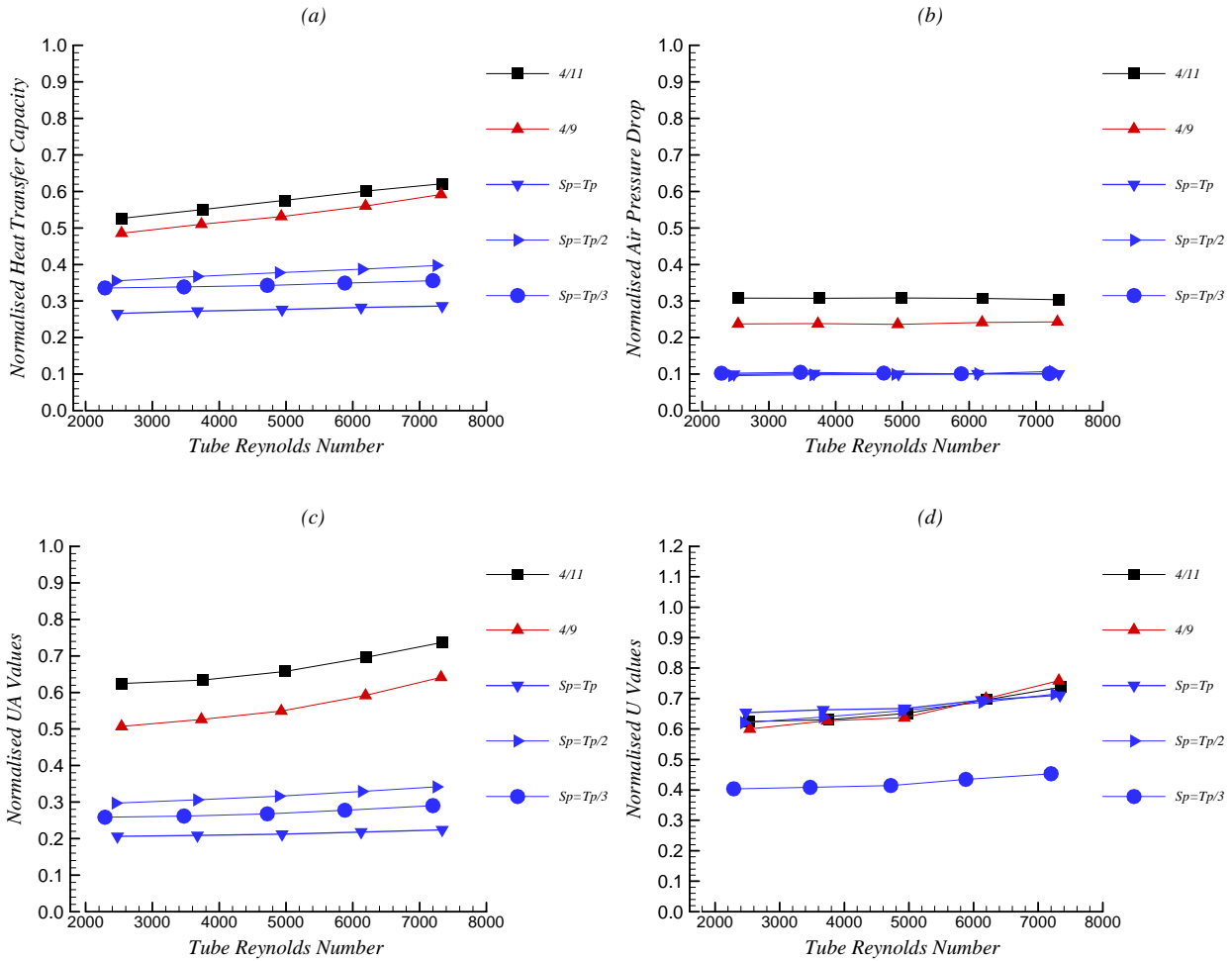
Figure 6.5.2 Performance comparison of the standard louvre coils and the three Tube Strut Heat Exchanger prototypes at inlet air velocity of 2.9m/s
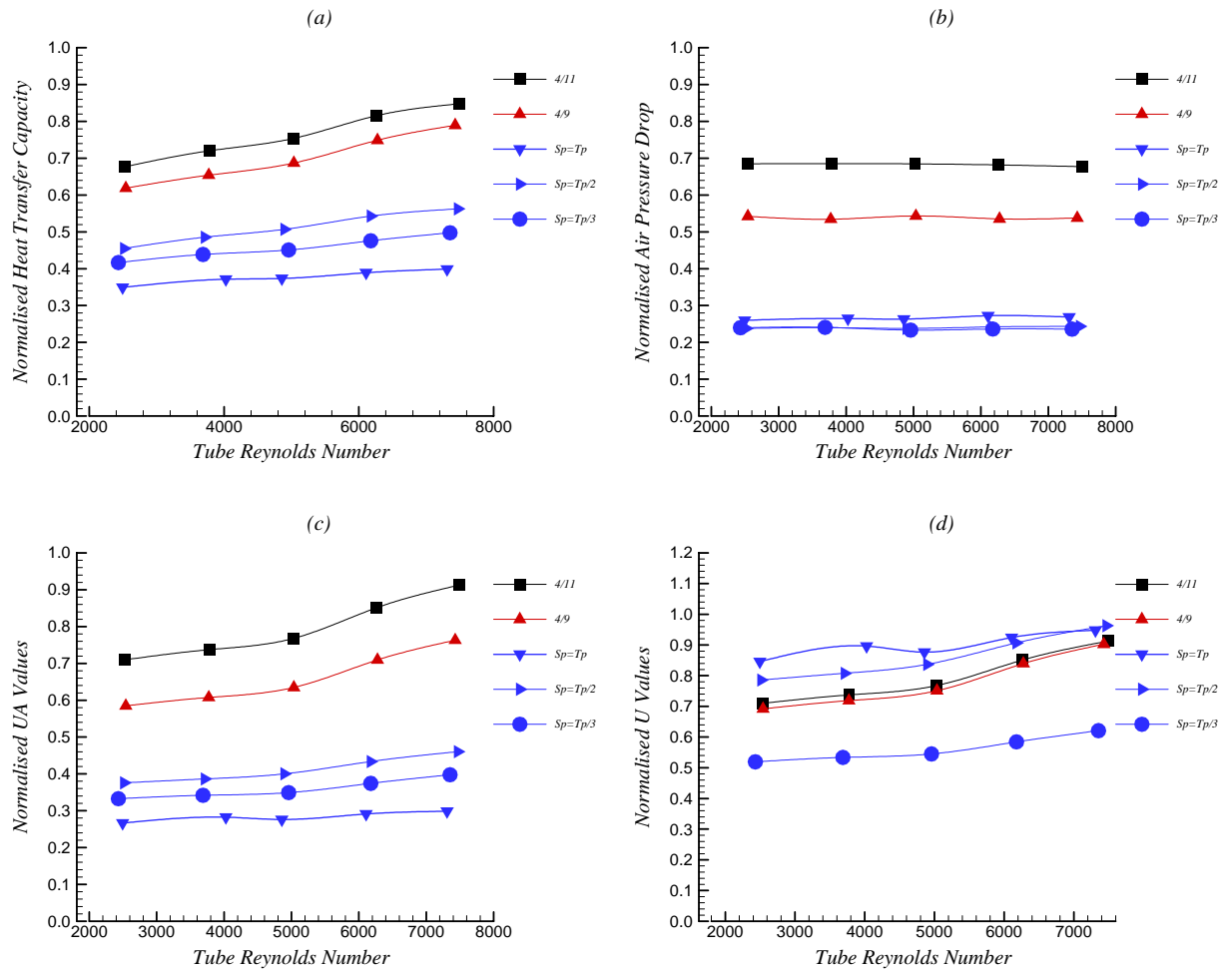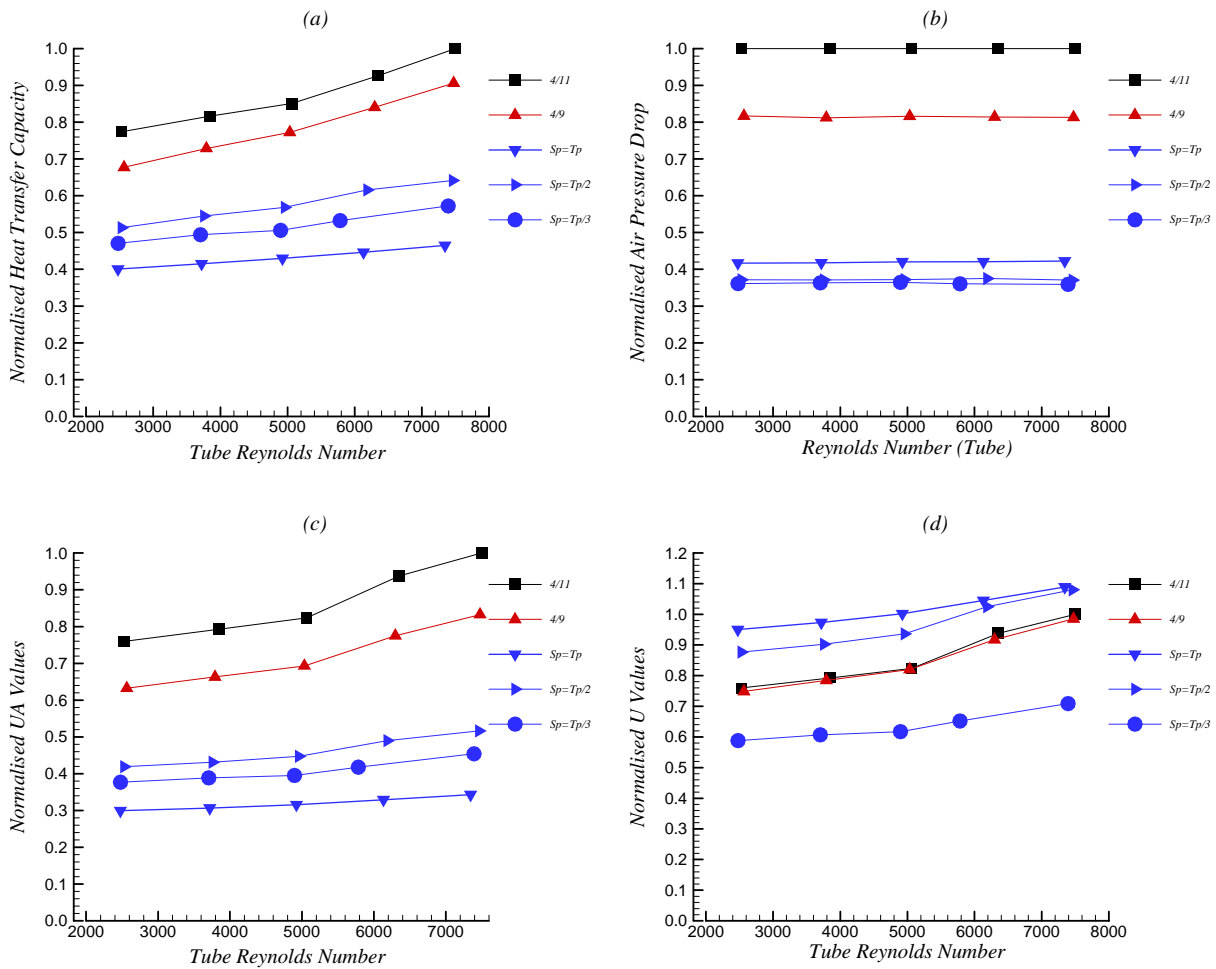
Figure 6.5.3 Performance comparison of the standard louvre coils and the three Tube Strut Heat Exchanger prototypes at inlet air velocity of 4.8m/s

Figure 6.5.4 Performance comparison of the standard louvre coils and the three Tube Strut Heat Exchanger prototypes at inlet air velocity of 6.3m/s

It is interesting to note that at an air velocity of 2.9m/s the graph of U values in Figure 6.5.2(d) all collapse onto the same curve with the exception of prototype 3. This deviation from the general trend implies that the performance of this coil was diminished compared to the design potential, possibly as a result of excessive contact resistance as well as disorientated struts, resulting from the problematical fabrication. Apart from this, the trends observed are similar between the three velocities tested, but the case of 6.3m/s air velocity provided a greater range of comparison, and these graphs are discussed below.

In general, when considering the graphs in Figure 6.5.4(a) and (b), the capacity of the three prototypes is approximately 45-65% of the 11fpi coil, while their respective pressure drop is approximately 38-42% of the 11fpi coil. Thus these prototypes demonstrate superior effectiveness to that of the louvre fin coils.

For the same cross sectional area, the heat transfer capacity of all the prototypes was lower than that of the standard coils at all water flow rates and air velocities. Out of the prototypes however, the strut spacing case of $Sp=P_t$, had the lowest capacity. This is in spite of this configuration of struts arranged to utilise the optimum array parameter. The thick struts should facilitate the highest generation of spanwise turbulence, and the wide strut spacing should permit prolonged existence of the vortices once they have been generated. However the strut spacing is such that there are too few to provide the necessary heat transfer surface area, as well as maximum number of leading edges to competitively enhance heat transfer when compared to the standard coils.

Doubling the number of struts to $Sp=P_t/2$ showed an improvement in capacity over the former case by a factor of approximately 1.4. The fact that the capacity did not double in proportion to the increase in strut quantity demonstrates that the convective heat transfer coefficient h_a has diminished. The reason for this reduction is clearly as a result of smaller vortex scales shed from the thinner struts, and possibly the quenching of vortices due to mechanical blocking and viscous dissipation along the strut sides.

The reduction in h_a is even more severe when trebling the number of struts to $S_p=P_t/3$. Although the performance has also improved (in comparison to $Sp=P_t$) by a

factor of 1.2, it is poorer than that of $Sp=P_t/2$. Presumably the thin struts do not shed vortices with the intensity that their thicker counterparts are known to do. Indeed, it is possible that they do not shed vortices at all. Furthermore, the narrow flow paths may be suppressing turbulence, and laminarizing the flow. Quite possibly, any capacity increase over the case of $Sp=P_t$ is due only to the increase in surface area and the number of leading edges.

If one examines the air pressure drop comparison, the pressure drop of each prototype is similar, and considerably lower than that of the two standard coils. The prototypes have a similar pressure drop even though the number of struts is doubling or trebling as the case may be, since the thickness of the struts is decreasing in each case. The pressure drop of each coil consists of the contribution of bluff body drag due to the frontal area of the struts, and a viscous drag along the sides of the struts. The proportion of each contribution varies with the quantity and thickness of the struts.

The plots depicting the *UA* values show the same trends as those of the plots of capacity. However there is a greater spread between the curves particularly at the higher water flow rates. This demonstrates the effect of the increasing *LMTD* which is higher for the best performing coils and for the greatest fluid flow rates.

If the surface area of each coil is taken into account then the plots of *U* values are obtained. A comparison can be made of the overall heat transfer coefficient of each heat transfer surface configuration. The prototype with the widest strut spacing has the best overall heat transfer coefficient, followed by $Sp=P_t/2$. The two standard coils have similar *U* values, no doubt attributable to their identical surface configuration. This also indicates that for the fin spacing of 9fpi, since the flow is already laminar, reducing fin spacing to 11fpi makes no further detriment to the convective heat transfer coefficient. The *U* value of the prototype with $Sp=P_t/3$ falls far short of the other coils, as anticipated and discussed earlier.

A useful observation can be made by a comparison of goodness factors as plotted in Figure 6.5.5. In this plot any value above the straight unity reference line has a goodness factor greater than unity, and is a result of the coil having a greater heat

transfer capacity for a comparable pressure drop to that of the standard 4row11 fpi coil, which has a goodness factor of 1. All of the coils including the standard 4row9 fpi coil have goodness factors greater than unity or better goodness factors than the 4row11 *fpi* coil. Of all the coils tested, the prototype with $Sp=P_t/2$ has the best goodness factor.
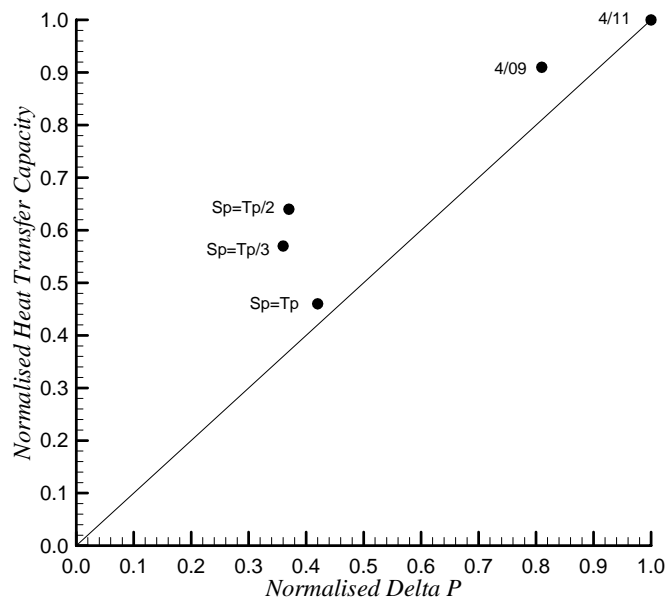

Figure 6.5.5 Goodness Factor comparison of the standard commercial coils and the 3 Tube Strut prototypes

6.6 Discussion

The experimental results appear to bear out the predictions made from the observations of the flow visualisation study. The prototype with the medium strut spacing had the highest capacity of the prototypes, and also demonstrated the highest levels of stream wise turbulence from the flow visualisation studies. This configuration, along with the other prototypes had considerably lower pressure drop than the standard coils. Unfortunately the combined parallel plate array with tube configuration is not competitive with the standard high performance coils. This is because the strut type heat exchanger has a much smaller surface area. Increasing the

number of struts to compensate for this lack in surface area is impractical due to the space restriction caused by the thickness of the struts. However the thickness of the struts is an important geometrical requirement for the generation of vortices. Other implications of the thicker struts, are increased material and weight. The only other way of increasing the strut surface area, without increasing the strut thickness, is to increase the strut width or chord length. In other words the leading and trailing edge of each strut could be extended past the centre line of each tube. This modification to the surface configuration was investigated using a series of CFD simulations, discussed in Section 6.8.

6.7   Numerical Simulation Comparison

Numerical simulations have been performed in order to compliment the flow visualisation results, as well as make performance predictions concerning various geometrical changes in the prototype configuration. The measured experimental results from the coil performance tests were used to validate the CFD models, and give credence to the outcome of the numerical predictions. Both the k-ε turbulence models and to a lesser extent, the LES turbulence models have been used. The aim of the CFD modelling is to gauge coil enhancement on a comparative basis, rather than to obtain exact performance values. Due to certain discrepancies between the model and the real physical case, exact performance calculation is not possible. For example in the model the tube temperature is assumed constant over the entire surface. In reality there is a temperature variation mainly along the length of the tube. Furthermore the simulation does not account for any contact resistance between the tubes and fins. Hence a discrepancy between experimental and simulated results can be expected.

The mathematical representation and general Numerical procedure used for performing the CFD simulations has been described in detail in Chapter 4. A tabulated summary of the boundary conditions can be found in Appendix III. This section reports on the CFD model used to simulate the performance of the three tube/strut heat exchangers, and investigates the effect of increasing the strut chord length, which is described in section 6.8.

6.7.1   Model Geometry

A three dimensional computational domain was developed for each case. Figure 6.7.1 is a sketch indicating the extent of the computational domain used for each of the tube/strut models at the three strut spacings. One could argue that the model could be simplified by halving it in height since it is symmetrical along the x-axis tube centre line. Then the top and bottom boundaries may have been specified as symmetry faces as done by Leu et al[51]. This may be valid for conventional tube fin heat exchangers where the fin spacing is narrow and the flow essentially laminar. However by virtue of the current design where the struts are widely spaced, horseshoe vortices are expected at the tube/strut intersections, as well as turbulence shed from the tubes themselves. This reasoning dictated that the top and bottom boundaries as well as the side boundaries, should be specified as periodic.

While horseshoe vortices may be generated in the real case, it is unlikely that a RANS type turbulence model will accurately predict the flow structure on a microscopic level. This is because the physical values of kinetic energy and turbulence energy are ensemble averaged. Hence these models have limited ability to simulate high pressure gradients and flow separation which are typically associated with vortex shedding. So although the overall effects of energy transport can be reasonably simulated, the finer details of localised flow structures most likely won't be represented. However since the major energy transport phenomena are simulated, reasonable estimates of heat transfer and pressure drop are possible.
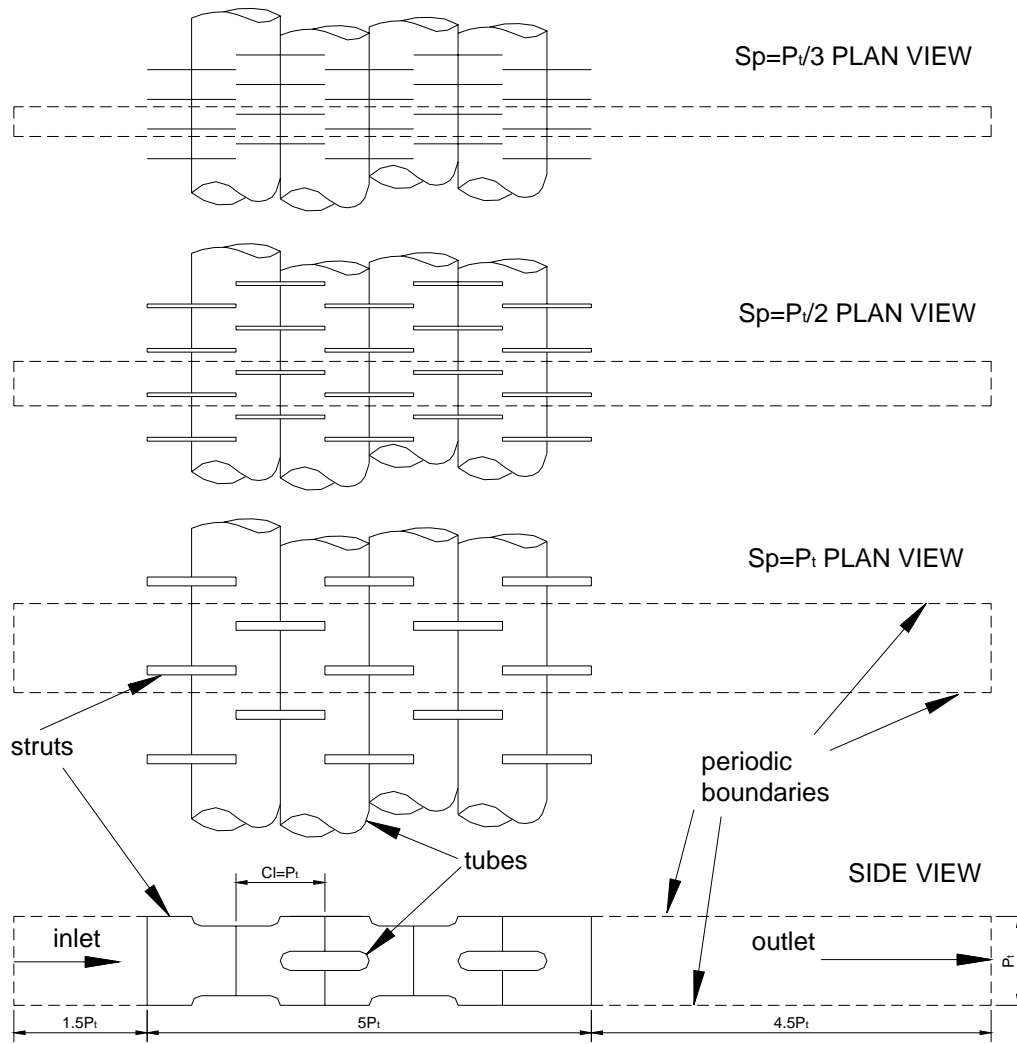
Figure 6.7.1 Sketch indicating the computational domain for each of the three Tube Strut models

The coil section consisted of a tube array 4 rows deep, and spaning between one transverse tube pitch P_t=12mm. The tubes were 12mm wide and 2.6mm across the tube flats. The length of the inlet section was $1.5P_t$, and that of the coil section including the struts was $5P_t$. The draught section had a length of $4.5P_t$. The extent of this computational domain was consistent for all the models. However the width of each model was equal to the corresponding strut pitch of each model. By reducing the width of the computational domain in proportion to the strut pitch for each model, suggests that any errors due to edge effects, would be likewise proportional for each model.

6.7.2   Mesh Structure

For the tube/strut models a structured mesh was used to discretize the volume as follows. The coil section of the domain comprising the tube array and the interconnecting struts was decomposed into several sections, in order to facilitate the generation of a structured mesh. Initially all edges were pre-meshed with a 0.2mm edge mesh. Prior to meshing the individual volumes, the top and bottom boundaries as well as the side boundaries of the domain were link-meshed. This ensures that the meshes on corresponding sides are identical, so that periodic boundary conditions can be implemented. Then the sides of the coil section were pre-meshed with a 0.2mm quad-pave face mesh. The quad-pave face meshes were then used as source faces to propagate a hex cooper mesh throughout each of the several volumes comprising the coil section. Note that the thickness of the cells along the domain width is 0.2mm.

Finally the inlet and draught sections were meshed with a sub-mappable hex mesh, consisting of cell size measuring 0.2mm by 0.4mm. A sketch indicating extent of the domain including the structured mesh is shown in elevation in Figure 6.7.2 and is typical for all three strut spacings.

6.7.3   Grid Independence Study

Rather than performing a perfunctory grid independence study for each computational domain, a discretionary selection of cell location central to the flow was believed to be is more functional. For the Tube/Strut computational domain, the mesh size located in the bulk fluid flow 0.2mm while specfic edges have been meshed with smaller mesh spacings. Looking at the domain in elevation shown in Figure 6.7.3, one can observe the quad pave mesh
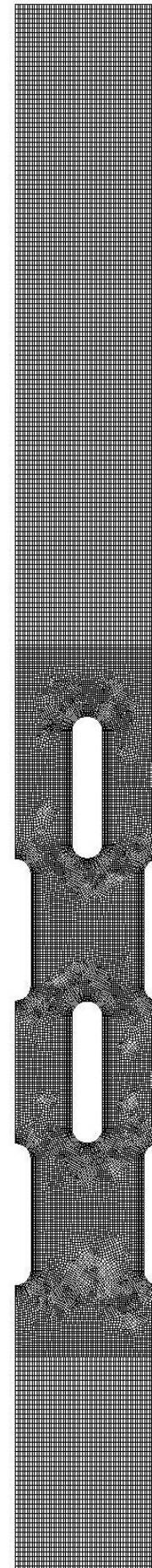
Figure 6.7.2 Sketch showing the structured mesh used for the range of tube/strut computational domains

structure including the structured boundary layers around the tubes. The first layer of the tube boundary layer mesh is 0.1mm, and along the tube semi-circle, the edge mesh is also 0.1mm. Hence there are approximately 40 elements around the tube semi-circles. Experience from initial modelling has established that this is a sufficiently fine mesh to capture the flow structure developing around the tube profiles. Hence there is little to be gained from refining the mesh in this plane.
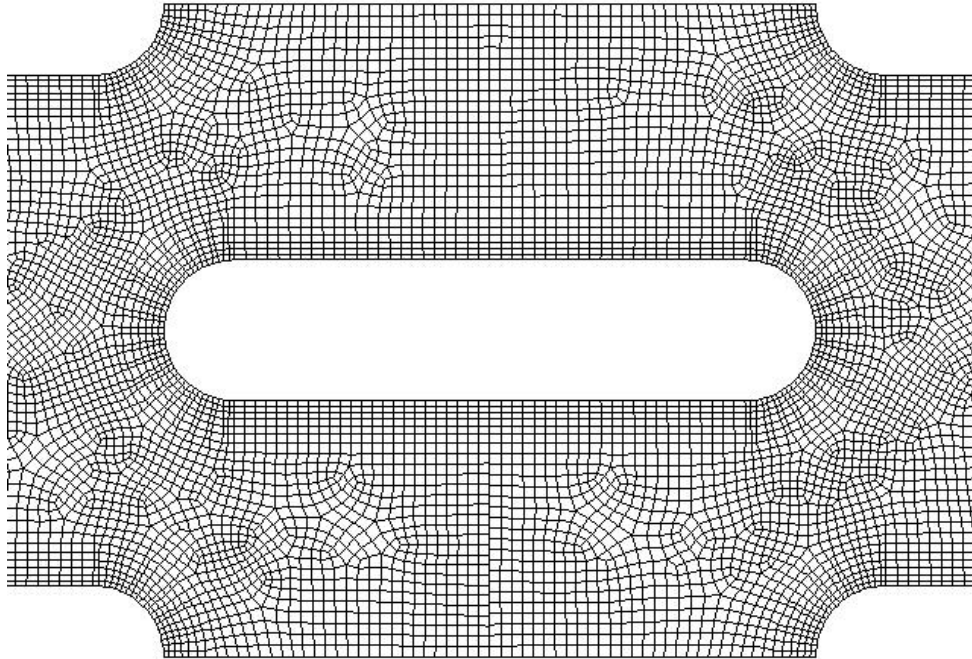
Figure 6.7.3 Close up view of the mesh around the tubes, showing the extent of Boundary Layer mesh

The critical dimension in this range of models is in the width where fluid transport may occur in the transverse direction. As the domain width decreases in line with the decreasing strut pitch, there will be fewer elements in this direction. Ideally the relevant cell size should scale proportionally to the thickness of the struts. It is important to have a sufficiently fine mesh in the transverse direction, in order to capture the effect of the fluid being deflected around the flat strut edges. It is this fluid deflection at the front of the struts which initiates the flow instabilities in the transverse direction, ultimately resulting in the span wise vortex shedding further downstream. The largest model ie $Sp=P_t$ is 12mm in width, and was meshed with a

0.2mm wide cell giving 60 cells. Since the strut thickness is 1.2mm, there are 6 cells across the strut width. In order to determine wether this is an adequate cell size to accurately simulate the flow structure, it is advisable to gauge the mesh size sensitivity. Table 6.2 sets out the results obtained by reducing the cell width by 0.05mm increments for the case of the middle size and smallest domains, the latter being expected to be most sensitive to cell size variation. This is particularly due for the case of Sp= $P_t/3$ where the strut thickness is zero and a greater error is likely to be incurred.

Table 6.2 Schedule of variation of parameters for grid independence study

Model	z-dim. mm	Cell number	Heat Transfer	Delta P	%change Heat Transfer	%change Delta P
Sp= $P_t/2$	0.2	849090	11.98	82.36	1.7	0.6
Sp= $P_t/2/2$	0.15	1040098	11.78	81.85	-	-
Sp= $P_t/3$	0.2	582885	14.01	62.09	5.7	4.1
Sp= $P_t/3/2$	0.15	761832	13.83	60.88	4.3	2.1
Sp=$P_t/3/2/2$	0.1	1148108	13.26	59.65	-	-

From Table 6.2 it can be seen that for the case of Sp= $P_t/2$ by reducing the cell size the heat transfer solution varies by only 1.7% and that of pressure drop by only 0.6%. Hence reduction in cell size does not produce any significant increase in accuracy. For the case of Sp= $P_t/3$ there is a greater sensitivity to variation in cell size, but still not prohibitively so. Even when reducing the cell size to 0.1mm, there is only a 5.7% error in heat transfer, and a 4.1% error in pressure drop. One can infer that if the 0.2mm transverse mesh size is used then the estimated error in heat transfer computation will be less than 6%, and will be less, as the model width increases. Similarly the error in computed pressure drop will be about 4% for the smallest strut spacing.

6.7.4   Boundary Conditions

Treatment of the boundary conditions in general has been described in section 4.4. The values of the initial boundary conditions have been summarised in Table 6.3, and sketched in Figure 6.7.4.

Table 6.3 Summary of the boundary conditions for the Tube/Strut range of heat exchanger CFD models

Boundary Conditions	Type	Values
Inlet	Velocity	6.3m/s,4.8m/s,2.9m/s
	Temp	313 K
	Turbulence Intensity	5%
Outlet	Pressure Outlet	Atmospheric
	Turbulence Intensity	15%
Top/Bottom	Periodic	-
Sides	Periodic	-
Struts(thick)	Solid	Brass(1.2mm),Copper(0.5mm)
Struts(thin)	Shell	Copper(0.076mm)
Tubes	Temperature	284.5 K
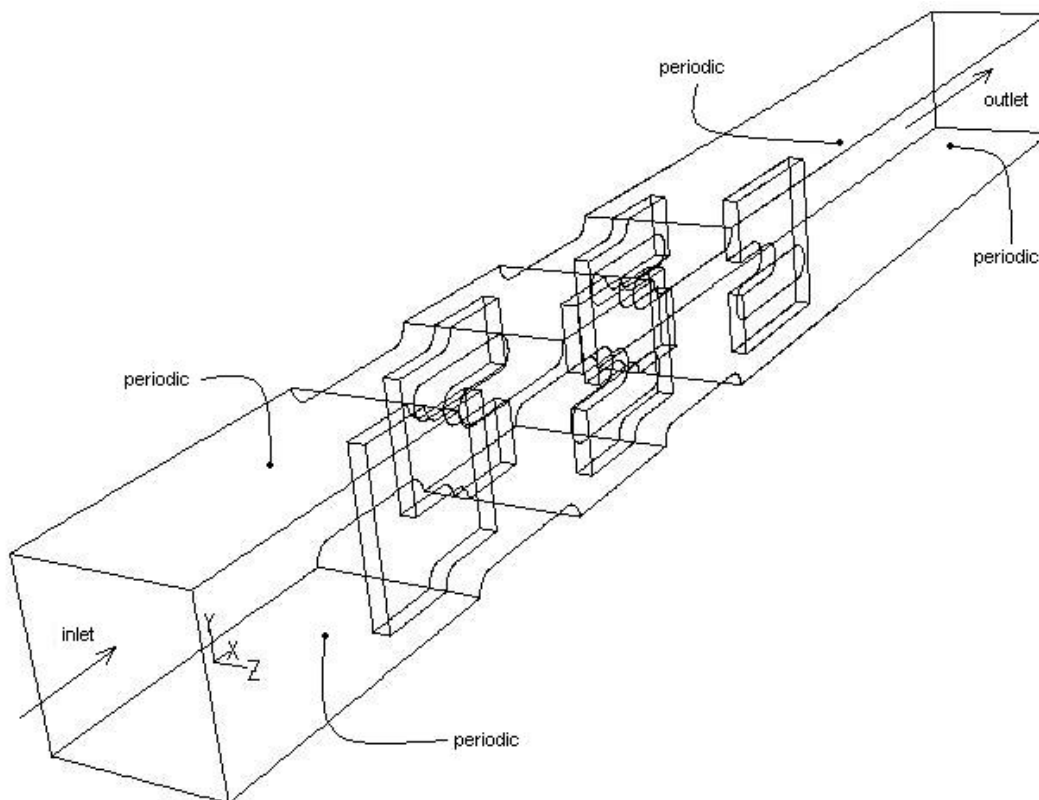
Figure 6.7.4 Sketch indicating the computational domain for the tube/strut model $Sp=P_t$, and indicates the location and designation of the boundary conditions typical for the tube/strut models

6.7.5   Near Wall Treatment

It may be recalled from Chapter 4 that the CFD code Fluent offers a range of wall treatment options. The most favourable option which has been adopted for all of the simulations is the enhanced wall treatment option. This is a two layer approach with enhanced wall functions. It is designed to accommodate meshes which may not be fine enough to adequately resolve the boundary layers close to the wall.

6.7.6   k-ε Turbulence modelling results

The following bar charts in Figure 6.7.5 and Figure 6.7.6 compare the results of the normalised heat transfer capacity and normalised air pressure drop for the CFD simulations, and the experimentally measured results. The CFD and experimental values have been normalised with respect to their respective maximum values obtained with the 4row11 coil in each case.
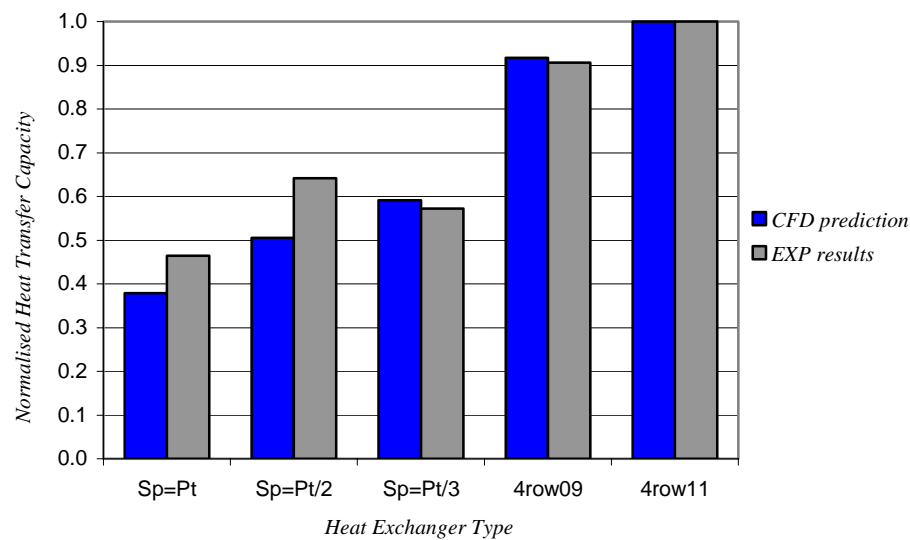
Figure 6.7.5 Bar chart comparing the normalised heat transfer capacity between the experimental results and CFD simulation of the Tube/Strut heat exchangers and the louvre fin coils

An inspection of the plotted normalised heat transfer values shows an excellent agreement in respective trends. The agreement is particularly good between the two commercial coils. The CFD model tends to under predict the heat transfer performance of the tube/strut coils by about 5-8%. An exception is seen for the case of

$Sp=P_t/3$ where the actual coil performance is much less than the increasing trend of the CFD prediction would suggest. This is undoubtedly as a consequence of the lack of adequate bonding and insufficient contact of the struts and tubes, as anticipated from inspection of the coil surface. The reader is reminded of the comments made in section 6.3.3, and observations of Figure 6.3.7 where it was observed that a reasonable percentage of the struts were bent and mal-aligned without making adequate contact with the tubes.
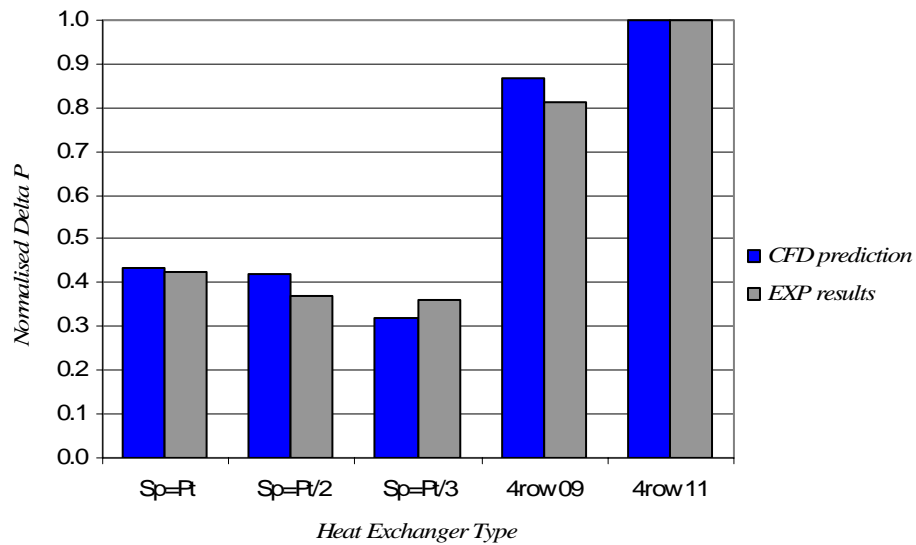
Figure 6.7.6 Bar chart comparing the normalised air pressure drop between the experimental results and CFD simulation of the Tube/Strut heat exchangers and louvre fin coils

The comparison of air pressure drop in Figure 6.7.6 also demonstrates a consistent trend between experimental and simulated results. In general the CFD models tend to over predict the air pressure drop by about 8%. It is noted however that for the case of $Sp= P_t/3$ the experimental results show a larger pressure drop by about 12% than can be expected judging by the CFD results. This is probably as a result of the loose fitting struts, the majority of which were twisted with respect to their intended alignment, and therefore causing additional pressure losses.

The close agreement in trends predicted by the CFD simulations and the experimental results can be a convincing argument in supporting the validity of the CFD models.

This also serves to provide confidence in using the model to predict performance due to other geometric variations in the heat exchanger surface. Apart from overall performance, other parameters can be locally assessed in order to investigate the influence of the geometry at particular locations throughout the model. For example it is useful to examine the surface temperature contours in order to identify where the majority of heat exchange occurs. The following plots in Figure 6.7.7 are temperature contour plots over the tube and strut surfaces for each of the models. Note that the temperature range is from 284.5K on the tube surfaces to 290K rather than the maximum inlet temperature of 313K in order to improve visual contrast.

Observing the temperature contours in Figure 6.7.7 (a) for the case of $Sp=P_t$ it is apparent that the temperature gradient throughout the struts is minimal. The thickness of the brass struts provides an unrestricted conduction path for heat flow. The heat in the air that is convected into the struts is rapidly conducted towards the tubes so that the entire strut surface approaches the temperature of the tubes. The lack of temperature gradient through the struts indicates that the strut material is not being utilised to its full conduction potential, and the air heat transfer coefficient is the limiting factor. The temperature gradients occurring in the case of $Sp=P_t/2$ in Figure 6.7.7 (b) are virtually the same. Although the conduction path has been reduced by virtue of thinner struts, apparently so has the air convection coefficient. The closer strut spacing and the thinner struts are less conducive to promoting any vortex generation. In both cases the amount of conductive material is far in excess of that required to balance the amount of heat introduced by air convection. In other words the vorticity levels are not high enough to augment the air side heat transfer coefficient sufficiently to match the conduction levels. In the case of $Sp=P_t/3$ in Figure 6.7.7 (c) the struts are many times thinner than the previous two cases greatly reducing the conduction path. As a result, in spite of the narrower strut spacing and diminished vortex generating propensity of the thinner struts, the air convection coefficient is not as limiting. It seems that the strut surface is more effectively utilised resulting in much greater temperature gradients across the strut surfaces, particularly in the front row of struts. It is clear that the front struts perform a significant amount of the overall heat transfer since they experience the greatest temperature gradient.
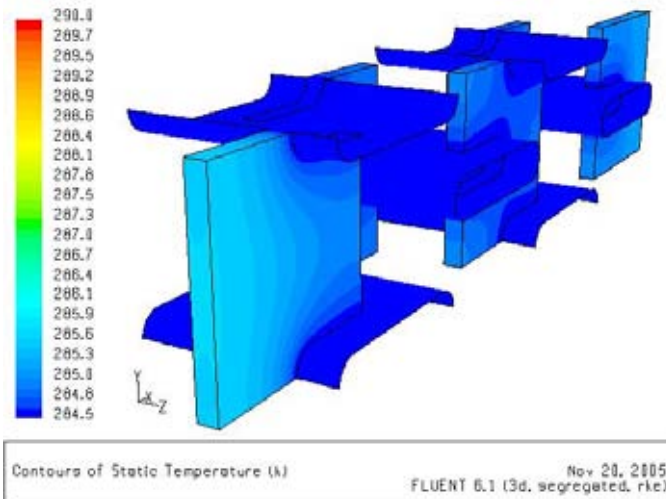
a) Sp=P_t
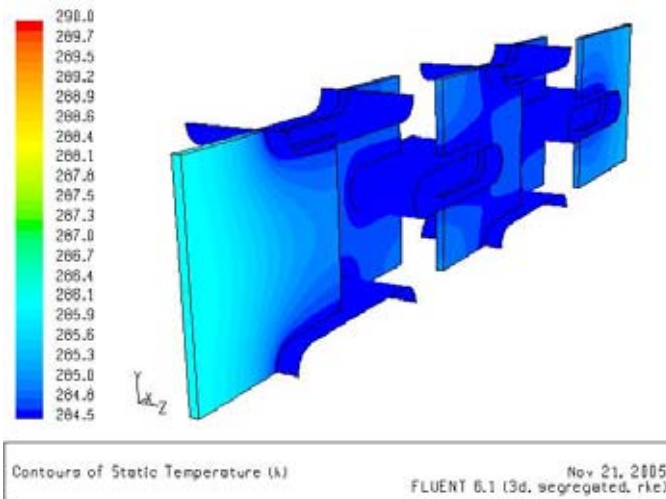
b) Sp=$P_t/2$
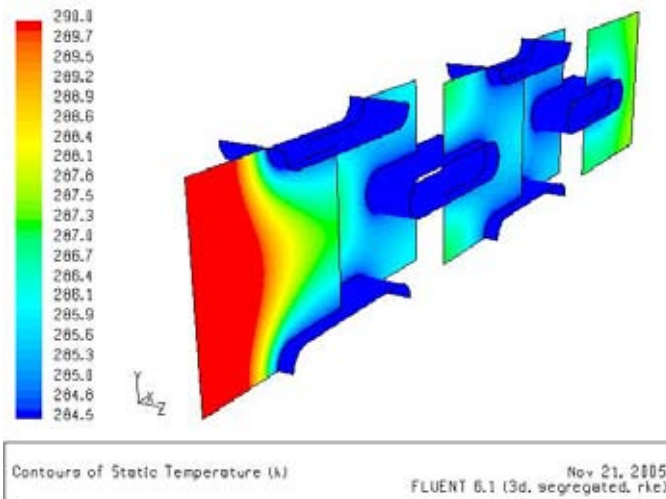
c) Sp=$P_t/3$

Figure 6.7.7 Plots of temperature contours over the tube and strut surfaces for each of the three cases

In this case the struts are more effective relative to the corresponding surface convection levels than in the previous two cases. This is not to say that they are more effective than the thicker struts. The thicker struts may actually conduct more heat in relative terms. In order to determine the heat transfer contribution of each strut thickness, plots of surface heat flux have been plotted in Figure 6.7.8. Note that the surface flux values are negative because the heat flow direction is into the strut surface from the inlet air. One can clearly see the 5 peak values of heat flux corresponding to the 5 strut leading edges, which are located at 12mm intervals along the x-axis, starting at an x-position of -18mm in each case.

It can be seen from Figure 6.7.8(a) for the case of the thickest struts, the majority of the surface heat flux values lie between 3000-5000 W/m^2 and the maximum flux values reach 10000 W/m^2 which occur at the first strut leading edge. From Figure 6.7.8(b) it is seen that most of the surface heat flux values lie between 2000-4000 W/m^2 and the maximum value at the first strut leading edge reaches 9000 W/m^2. Finally from Figure 6.7.8(c) it is evident that most of the surface heat flux values lie between 1000-3000 W/m^2 and the maximum value reaches 8000 W/m^2 at the first strut leading edge. However, even though the thickest struts have superior heat transfer performance, the small quantity of them limits overall heat exchanger performance.

It can be deduced from this collection of results that the thicker struts having a wider spacing have the best air side heat transfer coefficient. This implies that they have the highest level of transverse vorticity. However at this spacing there are too few struts to transfer sufficient heat, resulting in a poor overall performance. Reducing the strut thickness and spacing reduces the air convection but increases surface area. However it is clear that an optimum combination of strut spacing and thickness is not achievable which will make this heat exchanger configuration competitive with the louvre fin surface. Transverse vortex shedding does not increase convection levels sufficiently to compensate for the lack of surface area, as well as the reduction of leading edges.
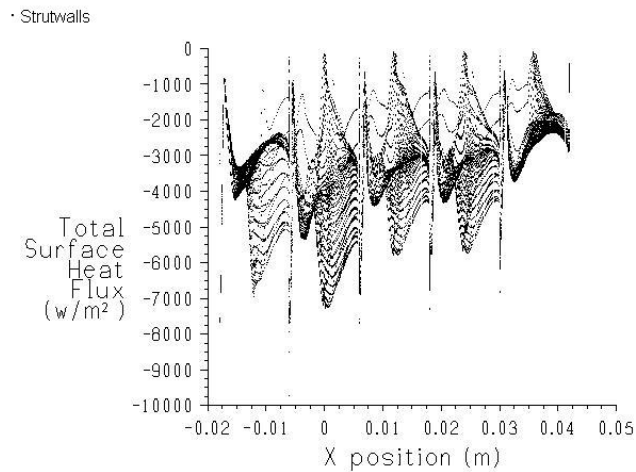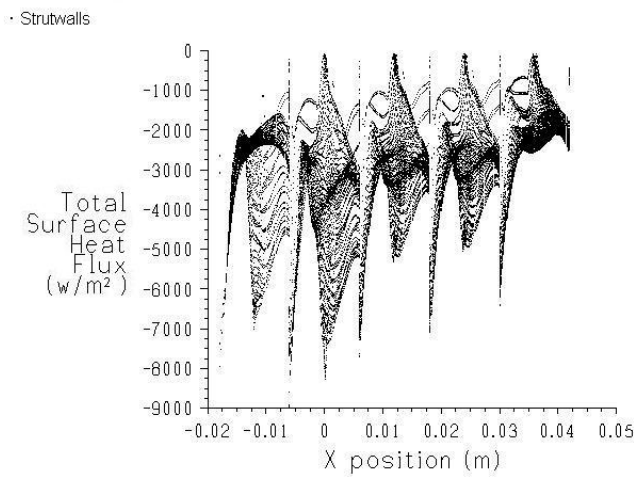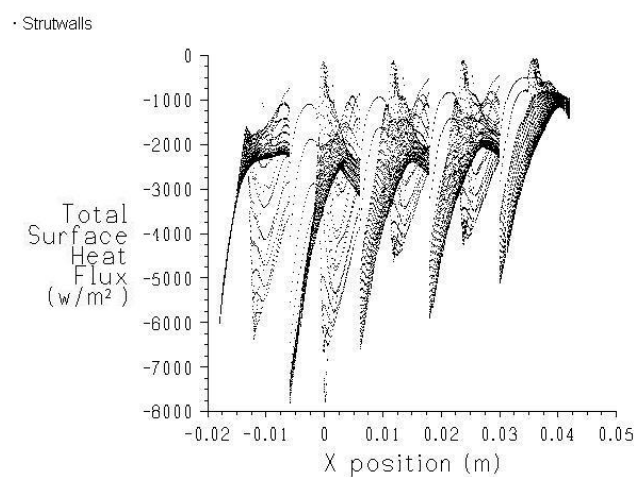
(a) Sp=Pt

(b) Sp=Pt/2

(c) Sp=Pt/3

Figure 6.7.8 Surface heat flux values plotted across the strut surfaces

6.7.7 LES Turbulence modelling results

The results in the previous section were interpreted within the context of assumptions about the level of transverse vortex shedding from the struts. However as stated in section 6.7.1 it is not likely that the details of the structure of any vortex shedding would be adequately conveyed using a RANS type turbulence model. It is thought that the thickness of the struts and particularly the bluff body effect on local flow phenomena is what determines the level of transverse vortex shedding. The flow visualisation study only focused on one strut thickness. Therefore it was decided to embellish the preceding study by performing corresponding LES simulations, particularly to determine if the parallel plate array having the thin struts is capable of exhibiting any transverse vortex shedding. Vortex shedding by tube bundle flows has been simulated with the large Eddy simulation technique for example by Hassan and Barsamian[63]. Their numerical predictions were consistent with experimental data and the "flapping" effect in the tube wake was fittingly captured.

For the simulations performed here, the appropriate time step size is based on the CFL Number[3]. Therefore considering the cell size and largest inlet velocity of 6.3m/s, an appropriate time step size was $1.0\text{x}10^{-5}$s. The following sequence of images, shown in Figure 6.7.9 to Figure 6.7.11 are relative vorticity plots on planes through firstly a plan view as well as a side view for each of the strut spacing geometries. The vorticity plots are at the three different inlet velocities and hence describe the development of the transverse vortex shedding quite adequately. The geometry in the case of Sp=Pt/2 is analogous to the geometry associated with the flow visualisation experiments described in section 6.2.3. The LES simulations have captured the mechanism of transverse vortex shedding where it occurs such that in the side views at least it closely resembles the results of the flow visualisation observations. In addition the vortex shedding from the struts can be simultaneously observed in the plan view.

---

[3] The definition of CFL Number has been provided in Chapter 4, which outlines the Numerical Procedure used to perform the CFD simulations.
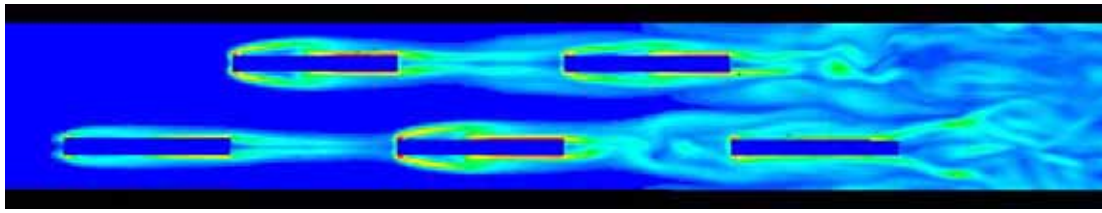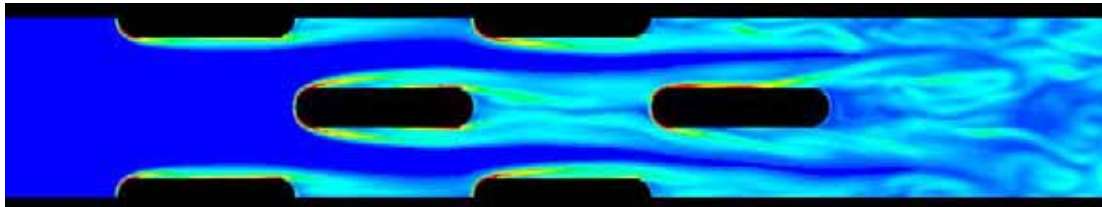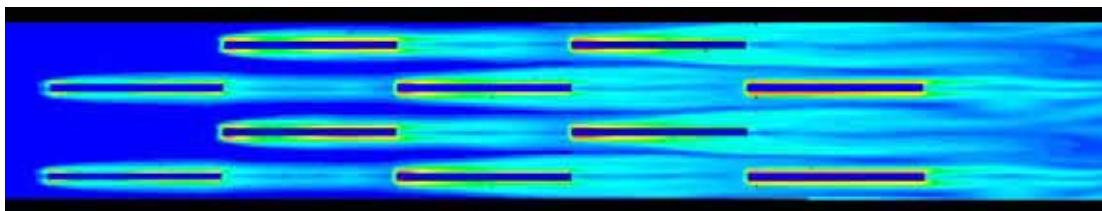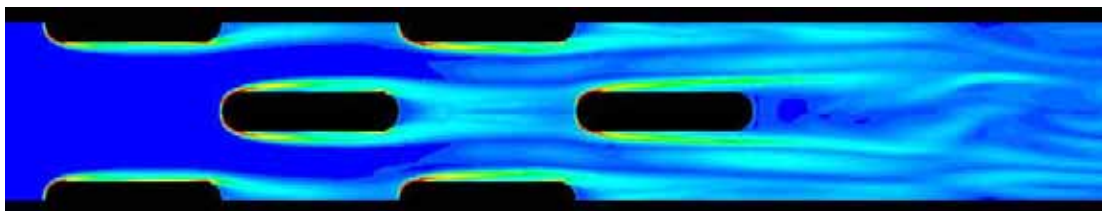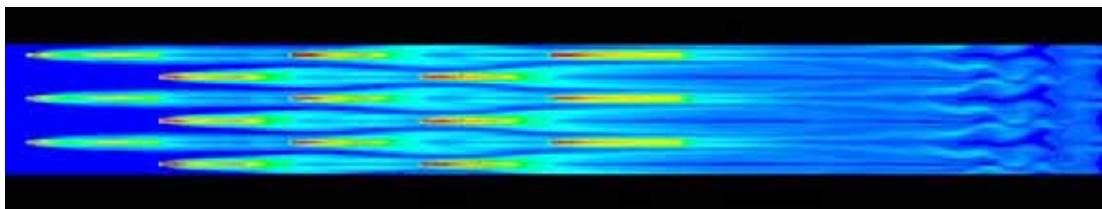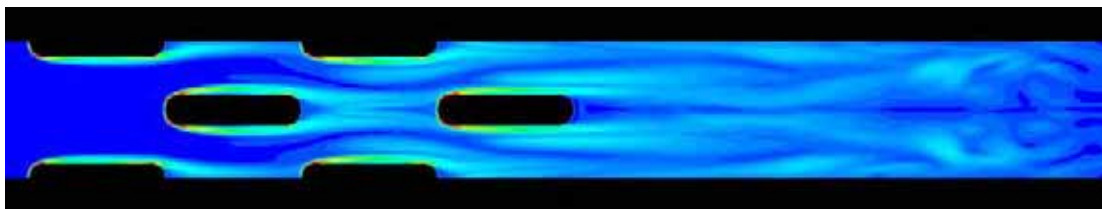
a) Plan view for Sp=P$_t$

b) Side view for Sp=P$_t$

c) Plan view for Sp=P$_t$/2 with one periodic repeat

d) Side view for Sp=P$_t$/2 with one periodic repeat

e) Plan view for Sp=P$_t$/3 with two periodic repeats

f)Side view for Sp=P$_t$/3 with two periodic repeats

Figure 6.7.9 Vorticity contours for an inlet velocity of 2.9m/s, CFL number 0.49, and vorticity range 0-20000(1/s). The Flow is from left to right.
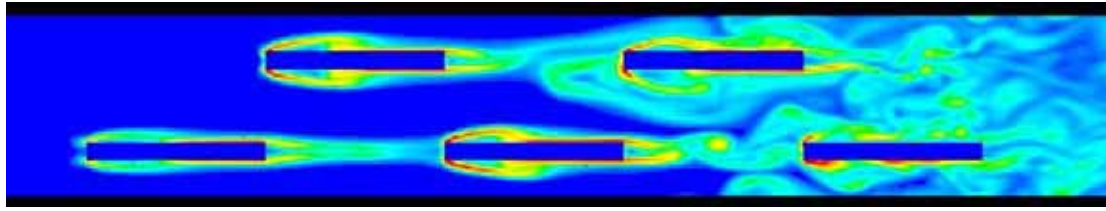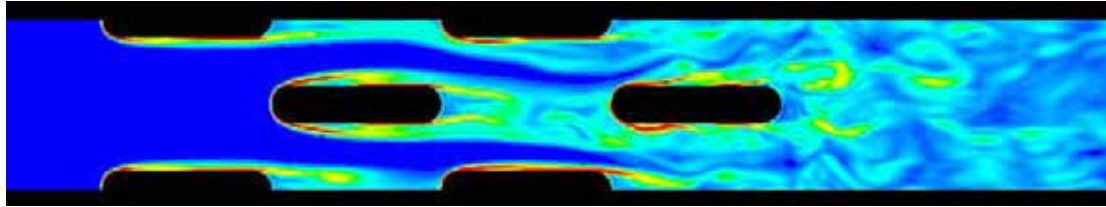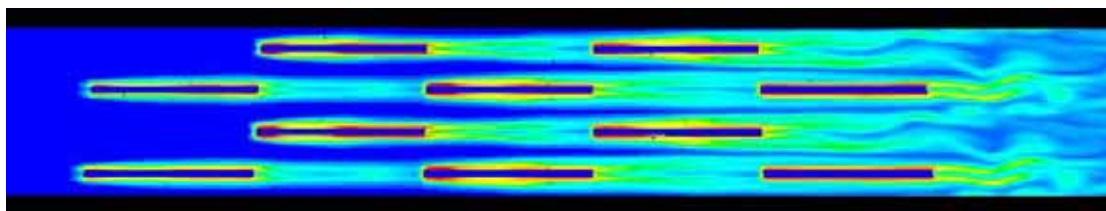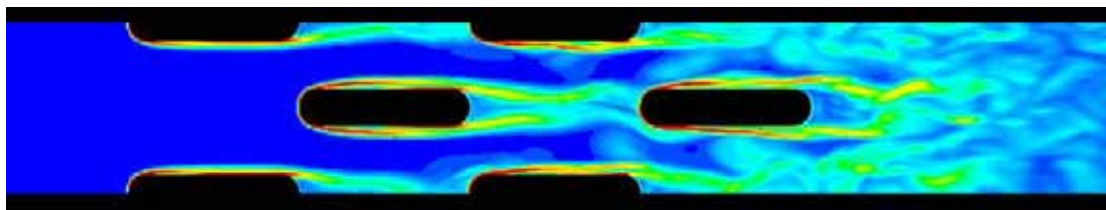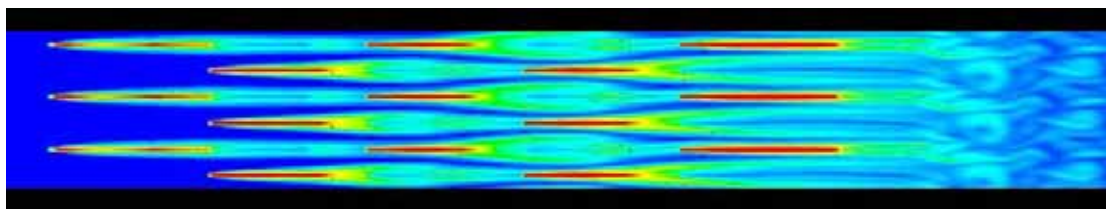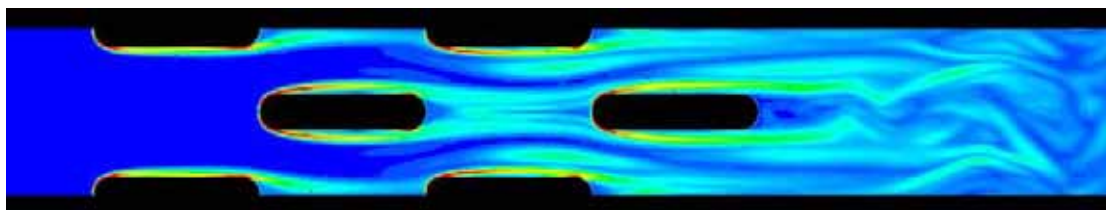
a) Plan view for Sp=P$_t$

b) Side view for Sp=P$_t$

c) Plan view for Sp=P$_t$/2 with one periodic repeat

d) Side view for Sp=P$_t$/2 with one periodic repeat

e) Plan view for Sp=P$_t$/3 with two periodic repeats

f)Side view for Sp=P$_t$/3 with two periodic repeats

Figure 6.7.10 Vorticity contours for an inlet velocity of 4.8m/s, CFL number 0.53, and vorticity range 0-24000(1/s). The Flow is from left to right.
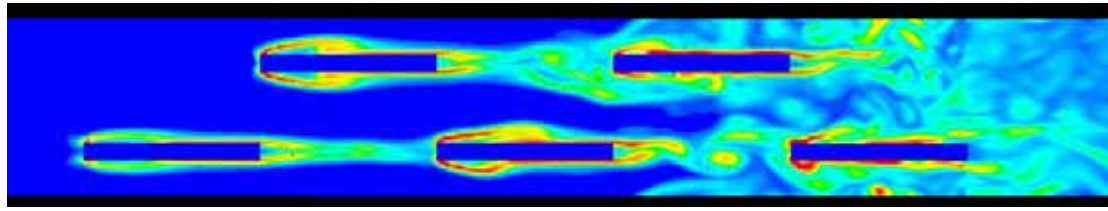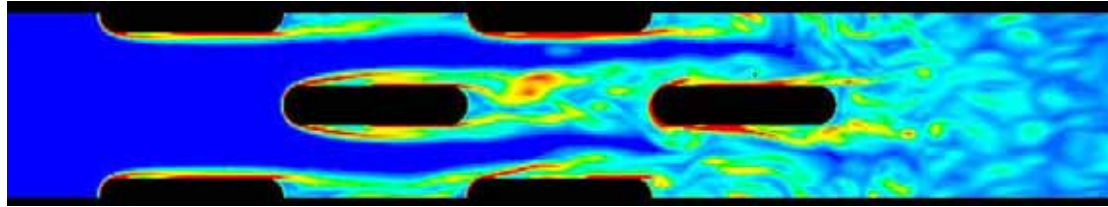
a) Plan view for Sp=P$_t$

b) Side view for Sp=P$_t$

c) Plan view for Sp=P$_t$/2 with one periodic repeat

d) Side view for Sp=P$_t$/2 with one periodic repeat

e) Plan view for Sp=P$_t$/3 with two periodic repeats
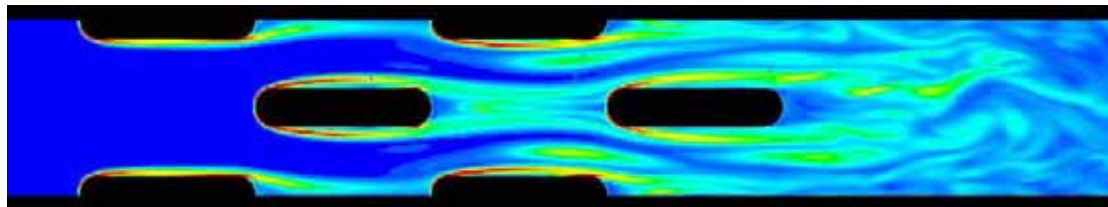
f)Side view for Sp=P$_t$/3 with two periodic repeats

Figure 6.7.11 Vorticity contours for an inlet velocity of 6.3m/s, CFL number 0.63, and vorticity range 0-28000(1/s). The Flow is from left to right.
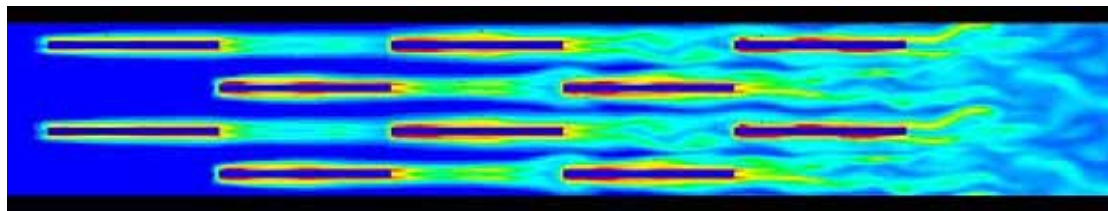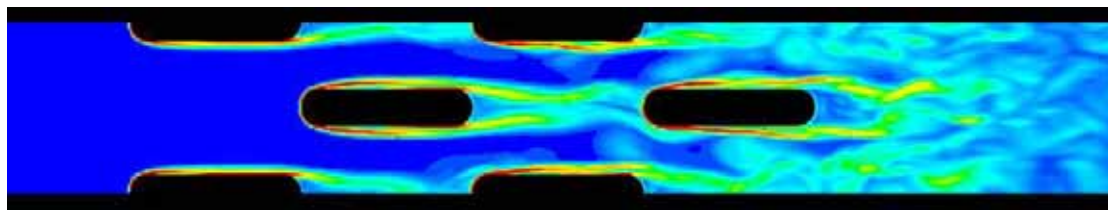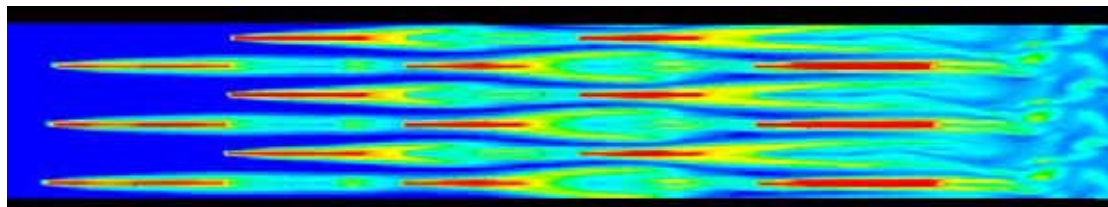
At an inlet velocity of 2.9m/s the thick struts are seen to initiate mild transverse vorticity shed from the 4th strut row. At the medium strut thickness some wake instability begins to show after the 4th strut row and particularly after the 5th strut row. The side view shows a lot less instability than the case of the thicker struts. In the case of the thin struts, the flow exhibits instability but this occurs far downstream from the exit of the strut array, but the flow becomes unstable about two strut chord lengths after the 5th strut row.

At an inlet velocity of 4.8m/s there is definite transverse vorticity shed from the thick struts at the 4th tube row. The medium struts show increased flow instability and observing the side view one can see mild vortex shedding from the second tube row. Even the thin struts have begun to show the presence of transverse vortex shedding from the last strut row.

At an inlet velocity of 6.3m/s there is distinct von Kármán type vortex shedding shed from the 3rd row of thick struts and to a weaker degree from the 2nd row. The medium struts also display von Kármán type wake structures after the 3rd strut row. The thin struts have begun to shed vortices but these only roll up some distance downstream.

These results demonstrate that it is not necessary to have struts with a finite thickness for vortex shedding to occur. As the flow passes down the channel between the thin struts, it is subject to viscous shear stresses which occur at a particular time interval depending on the inlet velocity and the longitudinal strut pitch. As the inlet velocity increases the frequency of the transient stresses increases until it coincides with that required for vortex shedding to occur. Of course if the struts have a form factor than the transient stresses are much larger resulting in more prominent vortices.

The graphics from the numerical simulations for the case of $Sp=P_t$ compare extremely well with the flow visualisations obtained from Smotrys *et al*[62]. Their visualisation of a plain parallel plate array is shown in Figure 6.7.12. von Kármán type vortices can be seen shedding from the struts at a Re number of 1480. Note that they used a different length scale for their Reynolds Number calculations. The correction has been applied to their results, and is displayed in brackets in the figure so that they can be directly compared to the foregoing results.

```
┌─────────────────────────────────┐
│                                 │
│            NOTE:                │
│  This figure is included on     │
│     page 164                    │
│  of the print copy of the       │
│     thesis held in              │
│   the University of Adelaide    │
│        Library.                 │
│                                 │
└─────────────────────────────────┘
```

Figure 6.7.12 Flow visualisation results of a plain parallel plate array at various Reynolds numbers. The numbers in brackets are the equivalent Reynolds numbers calculated using the same length scale as the foregoing results
Reproduced from Smotrys et al [62]

6.8   Effect of increasing strut chord length

It has been shown by the previous set of simulations that there are two mechanisms contributing to the performance of the tube/strut heat exchangers. The leading edge effect from the numerous thin struts is one, and the vortex shedding from the thick struts is the other. However it is not physically possible to combine both of these features in a practical sized coil. Furthermore neither of these features is independently capable of improving the heat transfer sufficiently to make the coil competitive with the standard louvre finned coils. Thick struts occupy significant space which limits the quantity that can be installed. Thin struts do not produce high enough levels of transverse vortex shedding. Neither construction has sufficient surface area to exploit any improvement in convection coefficient in each case.

The lack of surface area can be improved without restricting the free flow area by extending the chord length of the struts in the flow direction. This would have the additional advantage of increasing the tube/strut contact area and hence improve heat

conduction from the struts. On the other hand increasing the strut chord length causes overlap of the struts. This creates definite flow channels and hence limits the prospect of sustaining three dimensional vorticity. The numerical investigation was extended in order to assess how much additional strut chord length is required to achieve the target heat transfer performance.

6.8.1 Model Description

According to the previous results the model with the strut spacing of $Sp=P_t/3$ had the highest heat transfer performance. The simulation however was not negatively impacted by contact resistance which was experienced by the real prototype. Contact resistance aside, this configuration has the best expectation of increased heat transfer performance by increasing the strut chord length. Therefore the simulations are based on the narrowest strut spacing. Simulations were performed for models having strut chord lengths of 8mm, and 16mm, to compare with the standard case of 12mm. A chord length of 8mm was included in order to establish the existence of a trend, and to examine wether a negative chord overlap might permit a higher level of three dimensional vorticity. Figure 6.8.1 shows the extent of chord overlap for the case of a chord length of 16mm.
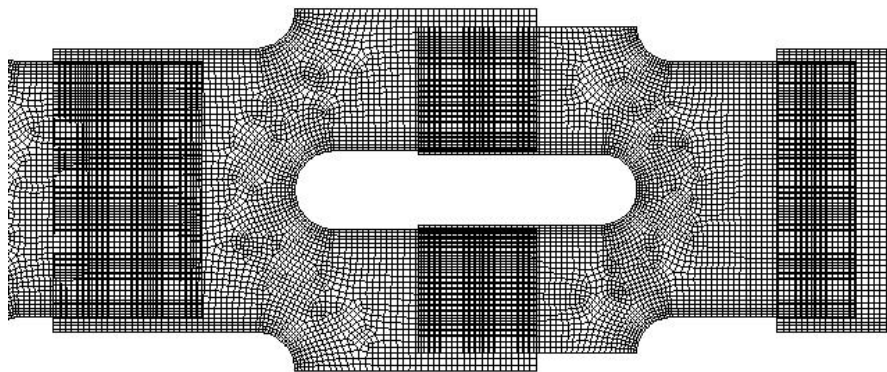

Figure 6.8.1 Sketch showing the extent of strut overlap for the case of
Sp=P_t and chord length CL=16mm

6.8.2   Simulation Results

The graphs in Figure 6.8.2 compare the heat transfer and pressure drop performance of the resulting simulations compared to that of the two the louvre fin surfaces. The plots have been normalised with respect to the CFD results for the standard 4row11 louvre fin geometry.

It is apparent that increasing the chord length to 16mm does not provide a sufficient increase in surface area to make this configuration competitive with the louvre finned coils. Although the strut surface area has increased by 33.3% the heat transfer performance has only increased by 10.2%. Although it appears that the increase in capacity with chord length is linear, it is actually closer to a polynomial relationship. This is because the average thickness of the boundary layer increases as the chord length increases and hence reduces the effectiveness of any additional length. The extrapolated curve indicates that a chord length in excess of 60mm would be required. Since this is longer than the standard fin length it renders this configuration impractical. In fact because the staggered transverse tube pitch is 24mm, the maximum chord length that can be accommodated in this parallel plate geometry is 24mm as well.

In spite of the increase in chord length, the air pressure drop remains substantially lower than that of the two louvre fin surfaces. At a chord length of 16mm it is only 30% of that of the 4row 11fpi coil.
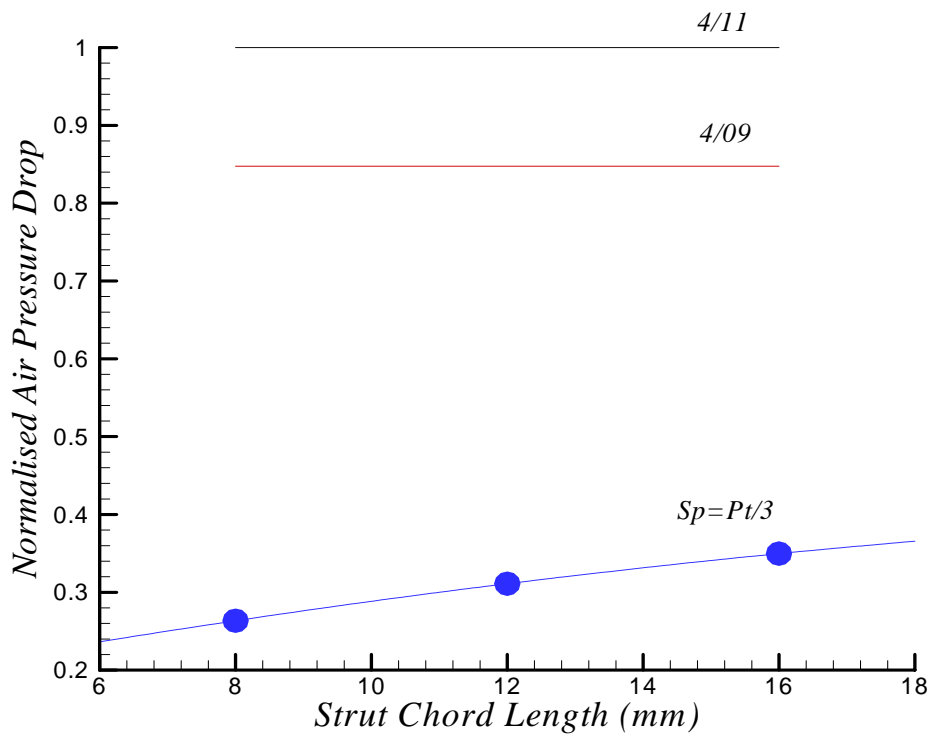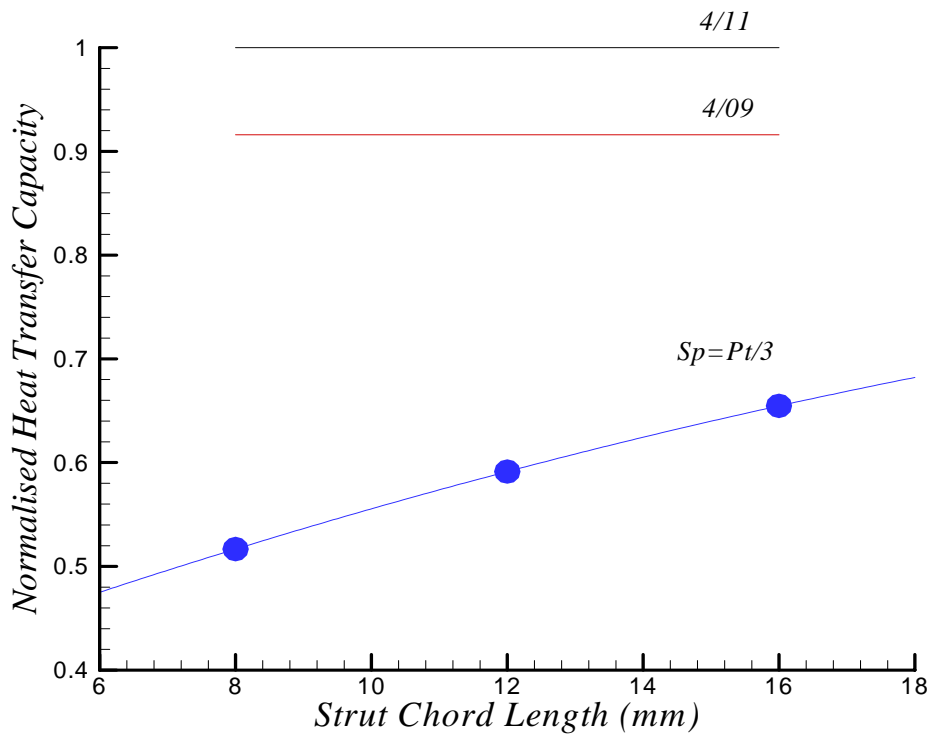
Figure 6.8.2 Performance comparison of Numerical Simulation results between the louvre fin coils and Sp=Pt/3 having varying Chord length. Note that in all cases the strut thickness is equal to the typical fin thickness i.e. 0.076mm

6.9   Concluding remarks

It has been demonstrated through flow visualisation, that when a tube array is combined with thick struts forming a parallel plate array, span wise vortex shedding occurs, and can be expected to enhance localised heat transfer. The experimental evaluation of working prototypes demonstrated that apart from the tube strut coil with the narrowest strut spacing, they have higher overall heat transfer (U) values than that of the louvre fin surfaces. Actually, the prototype with thin spacing may have performed significantly better, if the fabrication quality had been improved. The prototype with the thickest struts had the best normalised heat transfer coefficient compared to the two louvre fin surfaces. However the improvement in U is not sufficient to compensate for the lack of surface area resulting from the low strut density. The heat transfer performance increases as the strut density is increased, but not in proportion to the increase in surface area. This showed that the air heat transfer coefficient decreases as the strut thickness and spacing decreases. This is because the thin struts combined with the narrow spacing minimised the level of vortex shedding. Numerical simulations using an LES turbulence model indicated that vortices are more likely to be shed from thick struts, rather than thin ones.

The major advantage of this coil configuration is that all of the prototypes exhibited a very low pressure drop approximately 60% of that of the 4row 11fpi coil. This has the potential to be exploited in very low Reynolds Number applications, such as high altitude aircraft.

The experimental measurements facilitated the validation of a series of numerical models. A numerical simulation was performed to investigate the upshot of increasing the strut surface area by increasing the strut chord length. It was found that a reasonable increase in performance resulted, but not sufficiently to equal that of the louvre fin coils.

In general it can be concluded that transverse vortex shedding does not improve the air side convection coefficient sufficiently to be competitive

It is possible that the parallel plate array configuration may benefit from some additional means of generating stream wise vortices. As previously mentioned in Chapter 2, Smotrys et al[62] have investigated the performance of a parallel plate array which had triangular vortex generators located on the leading edge of the front struts. Their endeavours and the results from this chapter indicate that this principle can be incorporated in a heat exchanger configuration. Presumably they also concluded that parallel plate arrays alone do not produce sufficiently high levels of turbulence, and need to have other vortex generating devices to supplement their effectiveness. However, the combination of different types of vortices can lead to interference and actually result in a reduction in heat transfer.